ORNL/TM-2024/3604
M2CT-24OR1304043

Evaluation of Directed Energy Deposition and Laser Powder Bed Fusion Nickel-Based Alloys Process Application Envelopes Based on Performance, Process Economics, Supply Chain Risks, and Reactor-Specific Targeted Components

Sebastien Dryepondt
Holden Hyer
Amir Ziabari
Asa Monson
et al.

September 2024

OAK RIDGE National Laboratory

ORNL IS MANAGED BY UT-BATTELLE LLC FOR THE US DEPARTMENT OF ENERGY

ORNL/TM-2024/3604
M2CT-24OR1304043

Advanced Materials and Manufacturing Technologies Program

EVALUATION OF DIRECTED ENERGY DEPOSITION AND LASER POWDER BED FUSION NICKEL-BASED ALLOYS PROCESS APPLICATION ENVELOPES BASED ON PERFORMANCE, PROCESS ECONOMICS, SUPPLY CHAIN RISKS, AND REACTOR-SPECIFIC TARGETED COMPONENTS

Sebastien Dryepondt*
Holden Hyer*
Amir Ziabari*
Asa Monson†
Michael Mulholland†
Tate Patterson†
Michael McMurtrey†

* Oak Ridge National Laboratory
† Idaho National Laboratory

September 2024

Prepared by
OAK RIDGE NATIONAL LABORATORY
Oak Ridge, TN 37831
managed by
UT-BATTELLE LLC
for the
US DEPARTMENT OF ENERGY
under contract DE-AC05-00OR22725

CONTENTS

LIST OF FIGURES

LIST OF TABLES

ABBREVIATIONS

AM	additive manufacturing
AMMT	Advanced Materials and Manufacturing Technologies
BD	build direction
CAD	computer aided design
DED	directed energy deposition
EBSD	electron backscatter diffraction
EDS	energy-dispersive x-ray spectroscopy
FLiNaK	LiF–NaF–KF
GMA-DED	gas metal arc directed energy deposition
HN	Hastelloy N
HV	Vickers hardness
INL	Idaho National Laboratory
IPF	inverse pole figure
LPBF	laser powder bed fusion
LP-DED	laser powder directed energy deposition
NE	Office of Nuclear Energy
ORNL	Oak Ridge National Laboratory
SEM	scanning electron microscopy
STEM	scanning transmission electron microscopy
XCT	x-ray computed tomography
XRD	x-ray diffraction

ACKNOWLEDGMENTS

The authors would like to thank K. Carver, J. Moser, B. Abbott, D. Newberry, and T. Lowe at Oak Ridge National Laboratory for their help with the experimental work. The authors are also grateful for the assistance with the technical work at Idaho National Laboratory, including support from Q. Yang with the molten salt testing, N. Mohale with the creep testing, J. Simpson with the cyclic testing, and R. Seifert and M. Matos for assistance with the x-ray computed tomography. M. Ridley and P. Nandwana are also acknowledged for carefully reviewing the manuscript. This research was funded by the US Department of Energy Office of Nuclear Energy's Advanced Materials and Manufacturing Technologies program.

ABSTRACT

The goal of the Advanced Materials and Manufacturing Technologies (AMMT) program is to accelerate the deployment of new materials and manufacturing technologies into advanced nuclear-related systems. Although 316H stainless steel fabricated by laser powder bed fusion (LPBF) has already been identified as an alloy that could have a significant effect on various reactor technologies, many other materials and manufacturing techniques are being evaluated. For example, Ni-based alloys typically offer higher-temperature capabilities and good corrosion resistance compared with advanced stainless steels, and previous reports looked at three Ni-based alloy categories: low-Co alloys with a potential use close to the reactor core; high-temperature, high-strength alloys; and molten salt–compatible alloys. Because of the increasing interest in the low-Co 625 alloy for nuclear applications, the alloy was compared at Oak Ridge National Laboratory (ORNL) with alloys 617 and 230, which are two high-temperature, high-strength, solution-strengthened alloys. Hot cracking could not be suppressed for alloy 230, and this work showed that these cracks, which were elongated along the build direction (BD), had a drastic effect on the ductility of alloy 230 at room temperature when specimens were machined perpendicular to the BD. Cracking was not as significant for alloy 617 but still led to significant variation in ductility at room temperature along the BD. On the contrary, LPBF printing of crack-free alloy 625 was achieved using similar printing parameters, and the alloy seems to be a very promising candidate for various reactor technologies. The fabrication by additive manufacturing (AM) of the γ′-strengthened 282 alloy was also performed by LPBF at ORNL and by laser powder directed energy deposition (LP-DED) and gas metal arc directed energy deposition (GMA-DED) at Idaho National Laboratory (INL). Optimization of the printing parameters resulted in materials with low defect density, but the heat treatment needs to be further optimized to achieve full recrystallization and control the grain size. Characterization performed at INL on the LP-DED 282 alloy confirmed the presence of nano-size γ′ precipitates in the alloy as well as carbides at grain boundaries. The fabrication of larger builds by LPBF for mechanical testing led to significant local variations in flaw density, and x-ray computed tomography (XCT) scans of the alloy before and after creep testing at 750°C were carried out to establish a correlation between the flaws' volume fraction, creep ductility, and creep lifetime. Although the low creep and creep-fatigue behaviors of the LPBF 282 alloy compared with wrought 282 could be attributed to the presence of flaws, the effect of other microstructural features such as the grain size and the presence of brittle carbides at grain boundaries need to be further analyzed. Finally, single track experiments were performed at ORNL on the two alloys previously identified as good molten salt–resistant, Ni-based candidates: Hastelloy N (HN) and 244. Various laser parameters were considered, and cracking was not observed for either of the two alloys. Molten salt exposure at INL confirmed the compatibility of these two alloys in the wrought form with chloride and fluoride salts, and the excellent creep strength of wrought 244 makes the alloy a great candidate for molten salt components operating at temperatures $T > 700$°C.

1. INTRODUCTION

AM offers the ability to fabricate complex, near net shape components, reducing the need for machining, welding, or brazing during postprocessing [1]. Additionally, the US Department of Energy Office of Nuclear Energy's (NE's) Transformational Challenge Reactor program [2] demonstrated the first rapid component qualification paradigm using an advanced machine learning diagnostic tool fed by sensor outputs and health monitoring streams collected during LPBF printing [3–4]. Continuing this effort, the AMMT program [5] aims at the rapid qualification of new materials processed by advanced manufacturing technologies for current and advanced nuclear reactors. Stainless steel 316H fabricated by LPBF has been identified as a priority, and ongoing research revealed how digital manufacturing, innovative characterization techniques, and properties evaluation and modeling could accelerate the deployment of AM 316H [5–7]. Additionally, ORNL, INL, Pacific Northwest National Laboratory, and Argonne National Laboratory are collaborating on the identification of other advanced materials and

processes that could have a significant effect on nuclear technologies [8]. Pacific Northwest National Laboratory and Argonne National Laboratory focused their research on Fe-based alloys, and ORNL and INL investigated Ni-based alloys considering the following three alloy categories:

1. Low-Co alloys—With a potential use in the vicinity of the reactor core, three alloys were initially identified: alloy 800H, alloy 718, and alloy 625. Although 800H was the only code-qualified alloy, it was rapidly eliminated because of the lack of data on AM 800H and the difficulty in procuring 800H powder. Alloy 718 is already used in nuclear reactors [9], is a key AM alloy with a broad range of high-temperature applications [10], and was extensively discussed in previous reports [8, 11]. Unique long-term creep data presented in the previous report highlighted the potential of LPBF 718 for nuclear applications as long as the alloy ductility can be improved [11]. Alloy 625 was, however, identified as a higher priority for the AMMT program because of its higher-temperature capabilities and broader range of potential uses in current and advanced nuclear reactors. This report is therefore focused on alloy 625, and the alloy printability and properties will be compared with the printability and properties of high-temperature, high-strength alloys.

2. High-temperature, high-strength alloys—These alloys can potentially operate at temperatures >700°C, and the three alloys discussed in this report—alloy 617, alloy 230, and alloy 282—exhibit superior strength at high temperatures compared with alloy 625 in the wrought form. Alloy 617 is the only code-qualified Ni-based alloy for use in the pressure vessel [12], but very limited work has been published on alloy 617 fabricated by AM [13, 14]. The fabrication and characterization of LPBF 617 will therefore be discussed in this report. Alloy 230 [15] is another solution-strengthened alloy designed for improved balance between strength and oxidation resistance. Only a few AM studies have been reported on AM 230 [16–18], but the powder is commercially available. These two solution-strengthened LPBF alloys will be compared with the reference alloy, LPBF 625. Additionally, the γ′-strengthened Haynes 282 was fabricated using three different types of AM processes—namely, LPBF, directed energy deposition (DED), and wire-based AM. The alloy was selected because of its superior strength at high temperatures [19], feed stock availability, and growing interest from the AM industry [20]. Creep and creep-fatigue testing were performed on the alloy, and ex situ XCT characterization was conducted to shed light on creep deformation mechanisms.

3. Low-Cr alloys—These alloys are compatible with fluoride and chloride molten salts for operating temperatures above approximately 700°C. Two alloys were identified: Hastelloy N, an ORNL alloy specifically designed for molten salt applications [21], and alloy 244, a high-strength alloy originally designed for parts requiring low thermal expansion but with a Cr content of only 8 wt % [22]. While alloy 244 is expected to perform well in molten salt due to the low chromium content, little data exists, and so further down selection between Hastelloy N and alloy 244 was delayed until additional data could be examined.

A key goal of this collaborative report between ORNL and INL is to continue the downselection of Ni-based alloys and advanced processes initiated in 2023 based on their potential impact on current and advanced nuclear reactors.

2. SELECTION OF HIGH-TEMPERATURE, HIGH-STRENGTH ALLOYS

2.1 SOLUTION-STRENGTHENED ALLOYS 617, 230, AND 625

In the Larson–Miller plot in Figure 1, the creep strength of the wrought 617, 230, and 625 alloys were compared with creep data for wrought 230 and 625 from Haynes International [15, 23] and data for alloy

617 generated for the alloy code case [12]. The Larson–Miller parameter (*LMP*) was calculated according to the relation in Equation (1):

$$LMP = T \times (C + \log[t_r(h)]) \text{ with } C = 20, \quad (1)$$

with T equal to the temperature in kelvin, and t_r equal to time to rupture in hours.

As mentioned previously, although the creep strengths of alloys 230 and 617 were similar, the creep strength of alloy 625 was lower at low stresses and high temperatures. The goal of this study was to fabricate and characterize these three alloys to assess their performance when produced by LPBF.

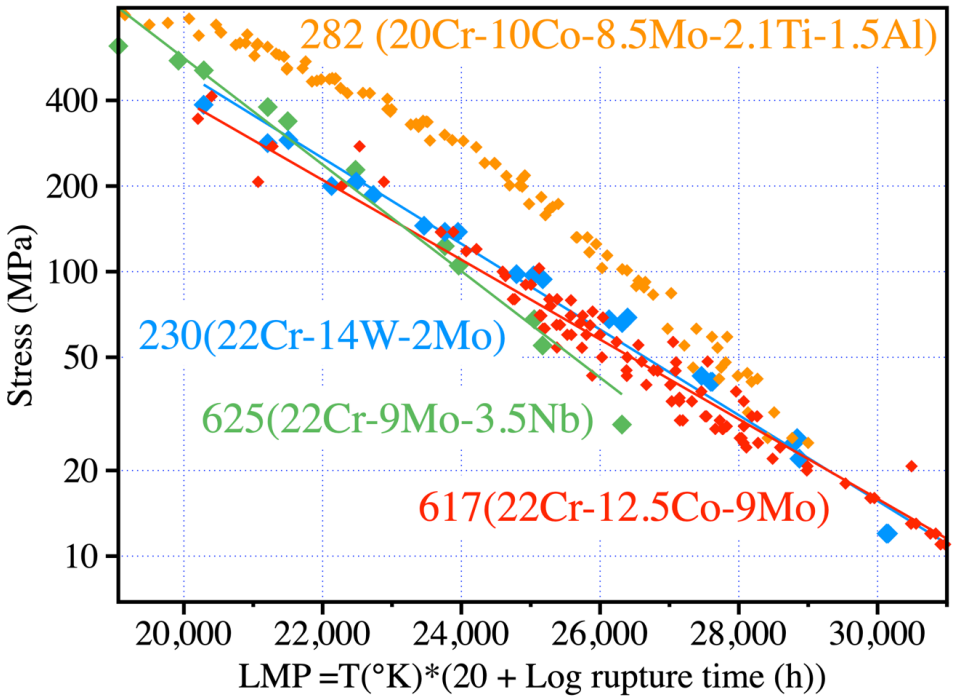

Figure 1. Larson–Miller plot comparing the creep resistance of five wrought Ni-based alloys [12, 15, 23, 23].

2.1.1 LPBF Parameter Optimization for Alloys 230, 617, and 625

A Renishaw AM250, fitted with a reduced build volume to limit powder consumption, was used to print the 230, 617, and 625 alloys. The powder chemistries provided by the powder manufacturers as well as chemistry measurements of the produced alloys are given in Table 1. Overall, limited variations were observed between the powder and alloy compositions. Small cubes with dimensions of 5 × 10 × 12 mm were initially fabricated to explore a broad range of printing conditions, and the parameter ranges are given in Table 2. For each condition, the energy density (*ED*) was calculated according to Equation (2):

$$ED = \frac{P}{\frac{p}{t+dt} \times h \times l} \frac{\text{J}}{\text{mm}^3}, \quad (2)$$

where P is the laser power, p the point distance, t the laser dwell time, dt is the delay time of the laser between pulses, h the hatch spacing, and l the layer thickness. After removal from the build plate, the density of the cube was measured using the Archimedes method, and the cube's relative density with

respect to the energy density is shown in Figure 2a. All the LPBF-processed alloys showed a very similar trend with a rapid increase of the relative density with increasing energy density up to 92 J/mm^3, followed by a plateau with a relative density of 98.7% for alloy 230, 99.3% for alloy 617, and 99.3% for alloy 625. As shown in Figure 2b, increasing the energy density above 92 J/mm^3 had an effect on the alloy grain structure with the disappearance of small grain areas and the exclusive presence of elongated grains along the BD for the cube fabricated with the higher energy density.

Table 1. Powder chemistries (wt %) for the 617, 230, and 625 alloys provided by the powder manufacturers compared with measured alloy chemistries

Alloy	Ni	Cr	Mo	W	Co	Fe	Nb	Mn	Si	Ti	Al	C	O	N	B	Other
617 powder	Bal.	22	9	—	12	—	—	—	—	—	1	0.05	0.01	0.01	—	—
617 alloy	Bal.	21.76	9.32	—	12.79	0.09	—	—	0.04	—	1	0.05	0.01	0.01	—	—
230 powder	Bal.	21	2	13	1	1	<0.5	0.6	0.4	<0.1	0.3	0.1	—	—	0.002	0.02La
230 alloy	Bal.	21.15	1.73	14	0.96	0.63	—	0.66	0.37	<0.1	0.3	0.07				
625 powder	Bal.	21.5	8.89	—	0.05	4.19	3.66	0.01	—	—	0.06	0.02	0.017	0.015	—	—
625 alloy	Bal.	21.41	9.49	—	0.07	4.03	3.61	—	—	—	0.12	0.02	0.02	0.01	—	—

Table 2. Parameters explored during printing of the three alloys

	Power (W)	Point distance (µm)	Dwell time (µs)	Hatch spacing (µm)	Layer thickness (µm)	Delay time (µs)
Range	150–350	55–110	60–180	60–120	60	10
Selected 92 J/mm^3	350	70	100	100	60	10
Selected 195 J/mm^3	250	40	140	80	60	10

Although a high alloy density could be achieved for the three LPBF alloys, cracking could not be suppressed for alloys 230 and 617, with a higher crack density for the LPBF 230 [18]. Figure 3 shows that many cracks were aligned with the BD and the grain structure. These cracks are likely due to hot tearing, and their presence has been discussed extensively for another solution-strengthened Ni-based alloy fabricated by LPBF—Hastelloy X (Ni–22Cr–18.5Fe–9Mo–2Co) [24–26]. The high residual stress caused by rapid cooling and thermal cycling during printing was determined to be a key factor for crack formation. The role of the alloy strength at very high temperature, microsegregation, and carbide formation have been discussed, which led to the conclusion that precise chemistry control, composition modification, or nanoparticle addition would be needed for the formation of crack-free LPBF Hastelloy X [24]. Zhao et al. added Zr in alloy 230 and showed that the alloy could be produced crack-free [16]. Thermodynamic calculations were initiated to assess the effect of chemistry modification on the printability of alloy 617.

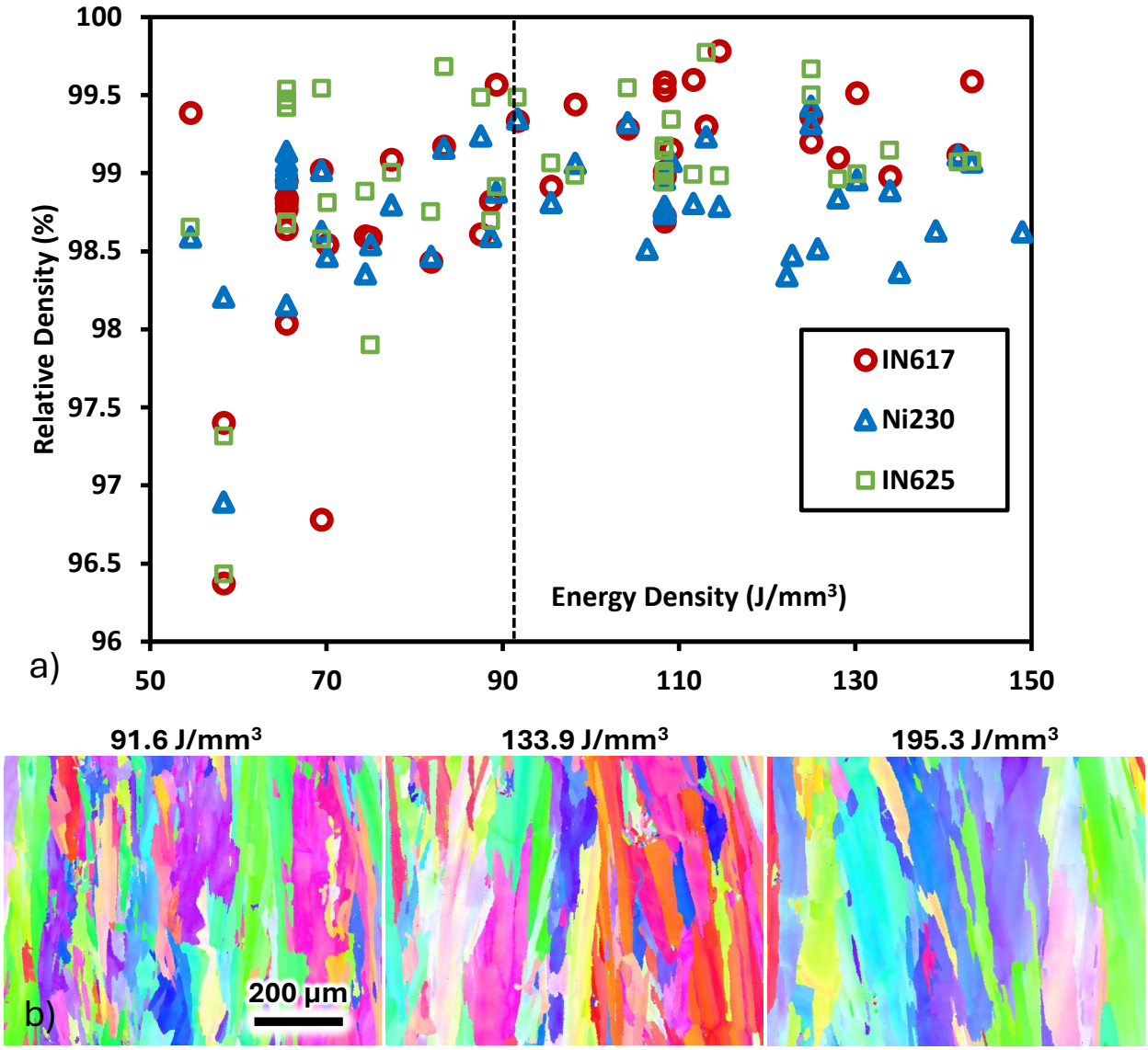

Figure 2. (a) Relative density measured using the Archimedes method versus printing energy density for LPBF 617, 230, and 625. (b) Electron backscatter diffraction orientation maps highlighting the effect of the energy density on the grain morphology for LPBF 230.

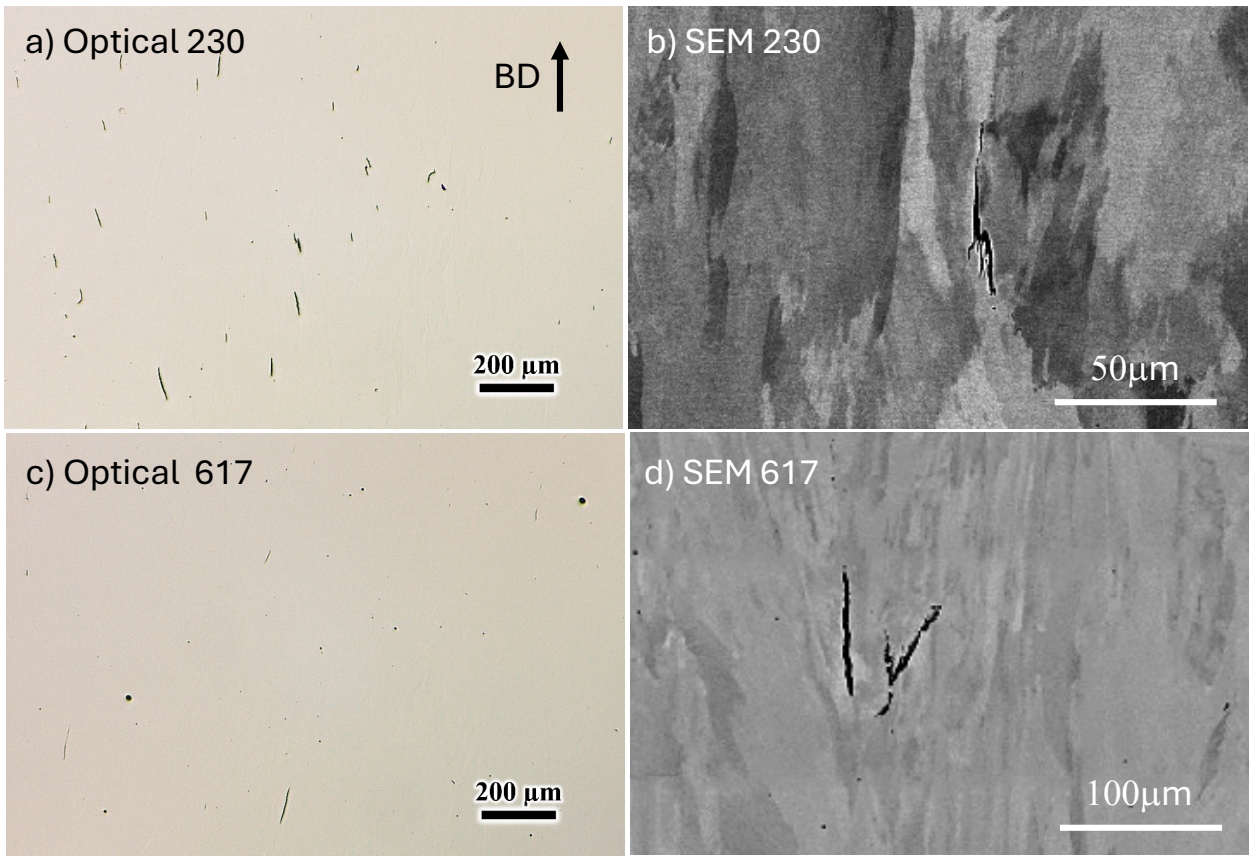

Figure 3. Micrographs of the LPBF 230 and 617 alloys showing the presence of cracks: (a) 230 optical, (b) 230 scanning electron microscopy, (c) 617 optical, and (d) 617 scanning electron microscopy.

2.1.2 Tensile Testing of Alloys 230 and 617

Two sets of printing parameters, detailed in Table 2, with corresponding energy densities of 92 J/mm^3 and 195 J/mm^3, were selected for the fabrication of 25.4 × 25.4 ×12.7 mm blocks of the LPBF 230 and LPBF 617, allowing the machining of small dog bone specimens with a gage length of 7.62 mm and a gage section of 2 × 2 mm. Specimens were machined along and perpendicular to the BD, and tensile curves at room temperature are given in Figure 4, with the properties summarized in Table 3 and Table 4 for LPBF 230 and LPBF 617, respectively. For the LPBF 230 alloy, excellent tensile properties were observed for the 92 J/mm^3 specimens machined along the BD, with average yield strength of 590 MPa, ultimate tensile strength of 869 MPa, and plastic deformation of 50%. These values are similar to the values expected for wrought 230 plates [15] except for a yield strength of only 383 MPa for wrought 230. High yield strengths are frequently observed for LPBF alloys because of the high dislocation density in the cell walls. Slightly lower yield strength and ultimate tensile strength were measured for the 195 J/mm^3 specimens, and further characterization is needed to evaluate the role of the grain and cell structures. A drastic decrease in ductility and moderate decrease in ultimate tensile strength were observed for the specimens machined perpendicular to the BD. The optical micrographs displayed in Figure 5 highlight the critical role played by the cracks in the alloy oriented perpendicular to the BD.

The results were quite different for the LPBF 617 alloy, with superior yield strength and ultimate tensile strength perpendicular to the BD compared with along the BD: 638 MPa yield strength and 847 MPa ultimate tensile strength perpendicular to the BD versus 549 MPa yield strength and 697 MPa ultimate tensile strength along the BD. Although these values are consistent with the ultimate tensile strength for

wrought 617 bars—769 MPa—the LPBF yield strength is again much greater than the yield for wrought 617—318 MPa—because of the high dislocation density into the cell structure walls. No effect of the energy density was observed perpendicular to the BD, with an average plastic deformation of 41%. On the contrary, a significant variation in plastic deformation was observed along the BD from 72% for the 195 J/mm^3 specimens down to 24% for the 92 J/mm^3 specimens. Characterization of these specimens is ongoing to understand the microstructural features leading to this ductility variation.

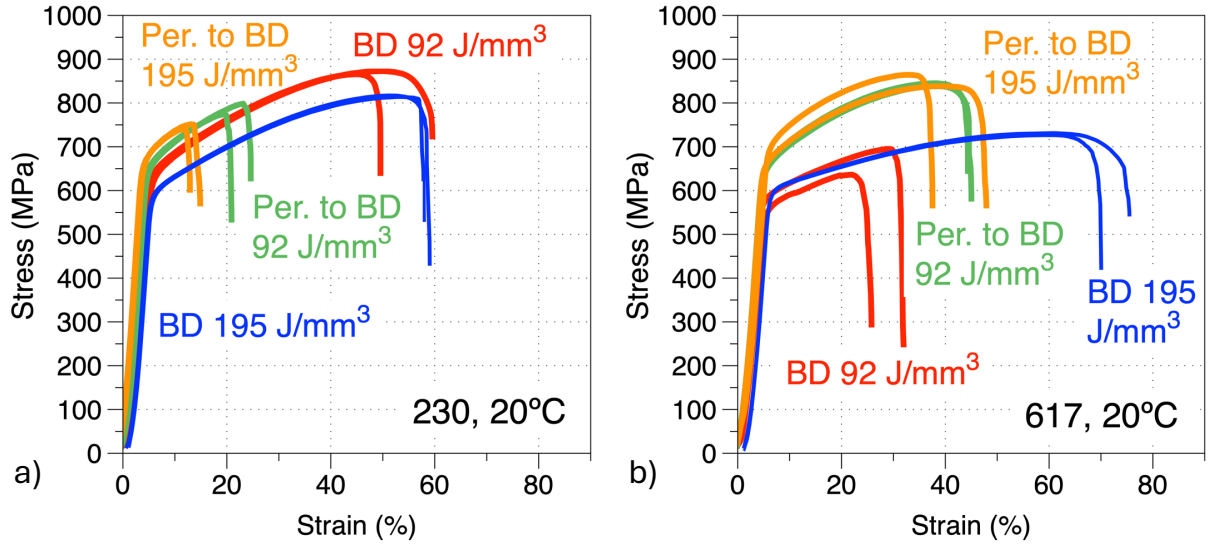

Figure 4. Tensile curves at room temperature along and perpendicular to the BD: (a) LPBF 230 and (b) LPBF 617.

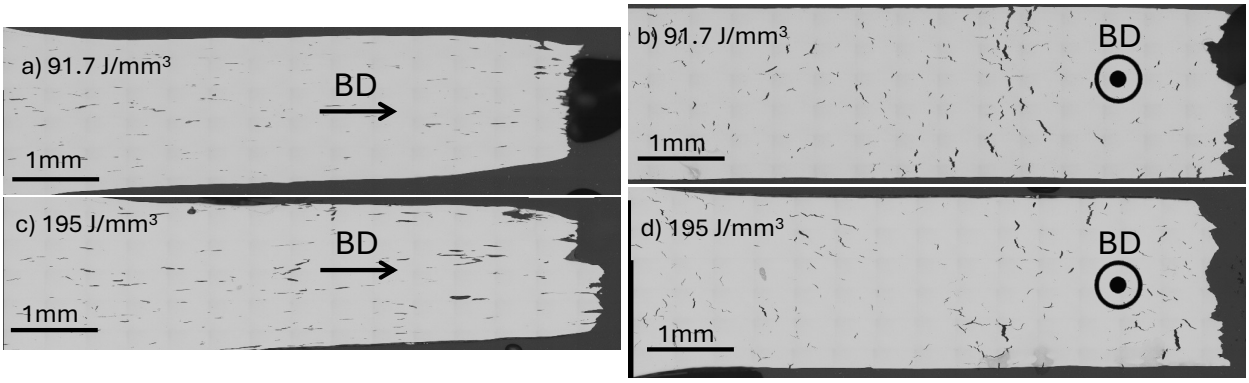

Figure 5. Cross-sectional micrographs of the LPBF 230 specimens after tensile testing: (a) 92 J/mm^3 along the BD, (b) 92 J/mm^3 perpendicular to the BD, (c) 195 J/mm^3 along the BD, and (d) 195 J/mm^3 perpendicular to the BD.

Table 3. LPBF 230 tensile properties at room temperature

Energy density (J/mm^3)	Orientation	Yield strength (MPa)	Ultimate tensile strength (MPa)	Plastic strain (%)
92	Perpendicular to BD	618.8	798.6	20.9
92	Perpendicular to BD	621.4	774.8	17.9
92	Along BD	588.6	873.0	54.8
92	Along BD	592.7	865.9	45.4
195	Perpendicular to BD	636.6	740.8	9.8
195	Perpendicular to BD	637.2	751.7	11.8
195	Along BD	560.8	817.4	56.5
195	Along BD	559.4	813.7	54.8

Table 4. LPBF 617 tensile properties at room temperature

Energy density (J/mm^3)	Orientation	Yield strength (MPa)	Ultimate tensile strength (MPa)	Plastic strain (%)
92	Perpendicular to BD	622.1	838.8	41.4
92	Perpendicular to BD	625.6	845.2	40.6
92	Along BD	520.6	636.5	24.2
92	Along BD	542.4	695.6	31.5
195	Perpendicular to BD	632.5	838.7	44.9
195	Perpendicular to BD	671.7	864.5	35.3
195	Along BD	567.1	731.4	72.1
195	Along BD	564.2	726.7	67.6

2.2 CONCLUSION ON HIGH-TEMPERATURE, SOLUTION-STRENGTHENED ALLOYS

Both the 617 and 230 alloys exhibited limited printability, and significant work would be required to produce these alloys by LPBF crack-free. Modification of the alloys' chemistries would likely be needed and would necessitate the purchase of custom-made powders. On the other hand, powder for alloy 625 is readily available and relatively affordable, and the 625 alloy offers a wide LPBF printing parameter window.

Additionally, although the creep properties of alloy 625 above 700°C are inferior to the properties of the 617 and 230 alloys, the strength of the alloy at a high temperature is significantly better than the strength of alloy 316H. The compatibility of alloy 625 with molten salt is inferior to the low-Cr, Ni-based alloys that will be discussed later but is again superior to the compatibility of alloy 316H. As will be discussed in a subsequent report, the overall high-temperature properties of alloy 625 make the alloy attractive to a broad range of nuclear reactors, and LPBF 625 will be the focus of this project in 2025.

3. EVALUATION OF ADDITIVE MANUFACTURING PROCESSES FOR HIGH STRENGTH OF γ′-STRENGTHENED 282 ALLOY

3.1 LASER POWDER BED FUSION

3.1.1 Material and Specimen Fabrication

The fabrication of alloy 282 by LPBF at ORNL using a Renishaw AM250 has been described in previous work [8, 11, 27] and will be briefly summarized here.

Haynes 282 powder was purchased, and the manufacturer's reported powder chemistry as well as chemistry measurements from two of ORNL LPBF rods are shown in Table 5. The powder and alloy chemistries were similar with small variations in the Cr and Al concentration. A key difference between the LPBF and DED powders was the relatively low Cr content for the DED powder, which was approximately 17 wt % versus 19 wt % for the LPBF powder. A Renishaw AM250 machine was used at ORNL to optimize the Haynes 282 printing parameters and to fabricate large rods and blocks for microstructure and mechanical properties characterization [8]. A hatch spacing of 86 μm, point spacing of 70 μm, and exposure time of 80 ms were determined to be optimum for the processing of Haynes 282 with a laser power of 200 W and a powder layer thickness of 60 μm [8]. The two large builds that were fabricated—one for ORNL and one for INL—are displayed in Figure 6. Each of the rods and rectangular blocks were engraved to ensure the data that will be generated can be integrated into the digital manufacturing approach. The build configurations were based on the standard tensile/creep specimens at ORNL and the standard tensile/creep and fatigue specimens at INL. The ORNL threaded creep specimens were 3.5 in. long, requiring 4 in. long specimens, and the INL smooth button head fatigue specimen was 6 in. long, requiring rods 6 in. long and 0.75 in. in diameter or plates 6 in. long and 0.75 in. thick. A list of the rods and plates used for microstructure characterization and mechanical testing is given in Table 6.

Table 5. Manufacturer-reported 282 powder and alloy composition for LPBF and LP-DED builds

LPBF composition (wt %)											
	Ni	**Cr**	**Co**	**Mo**	**Ti**	**Al**	**Fe**	**Mn**	**C**	**Si**	**O**
LPBF alloy 282 powder composition	Bal.	19.37	10.24	8.33	2.11	1.54	—	—	0.05	0.03	0.01
LPBF alloy 282 composition C4	Bal.	18.55	10.05	8.7	2.03	1.42	0.05	—	0.04	0.01	0.01
LPBF alloy 282 composition T4	Bal.	18.98	10.51	8.76	2.07	1.5	0.05	—	0.05	0.02	0.01
LP-DED alloy 282 powder composition	Bal.	16.92	9.35	8.23	1.95	1.52	0.22	0.02	—	0.08	—
LP-DED alloy 282 composition	Bal.	17.21	9.67	8.44	1.99	1.49	0.21	0.02	—	0.12	—

Table 6. List of the rods and plates used for microstructure characterization and mechanical testing

Specimen type	Designation	Laboratory
Creep/metallurgy	C1, C3, C5, T1, T3, T5	ORNL
Metallurgy	TV4, FV1, FV5, FV6, FV7, FV8	INL
Creep	CV2, CV3, CV-5 and TV1	INL

Fatigue and creep Fatigue	FV2, FV3	INL

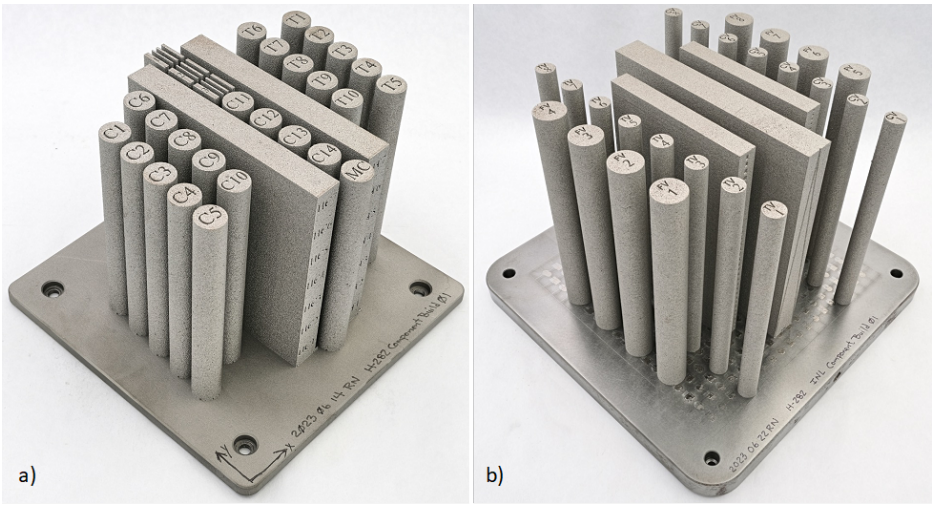

Figure 6. LPBF builds of mechanical test specimen blanks: (a) ORNL build and (b) INL build.

3.1.2 Material Characterization

3.1.2.1 Optical microscopy and flaws characterization

Six vertical rods were used at ORNL to machine 89 mm long creep specimens with a 6.35 mm gage section in diameter and 31.75 mm in length. The full sequence for creep specimen machining and annealing was as follows: 1 h at 1,180°C in flowing Ar, air-cooling, specimen machining, annealing for 4 h at 800°C under vacuum, and cooling in the vacuum furnace with flowing He. The leftover material from each rod was cross-sectioned for microstructure characterization, and Figure 7 shows optical micrographs of the T5 and C5 rods along and perpendicular to the BD, as well as T3 perpendicular to the BD and C1 along the BD. The C1 and T1 coupons were annealed for 1 h at 1,180°C in a furnace with flowing Ar followed by cooling in air. The T5 and C5 coupons were also annealed for 1 h at 1,180°C but then were heat-treated for 4 h at 800°C in a vacuum furnace to mimic the creep specimen full heat treatment. As highlighted in Figure 7, the density of flaws was significantly higher for the C1, C3, and C5 specimens compared with the T1, T3, and T5 specimens. As explained in previous reports, such a variation in flaws might be related to spatter particles during printing [8, 11]. Similar characterization was conducted at INL, and optical micrographs are presented in Figure 8.

The porosity near the bottom was measured to be approximately 2 area %. FV1 was then serial sectioned to study the variation in porosity throughout the sample height, and the porosity extended throughout the sample. The center slice was mounted and polished to quantify the porosity, which is shown in Figure 8b. The porosity was measured to be approximately 5%. Tensile blank TV4 was also sectioned near the build plate to check for porosity. This sample also had porosity at 0.7% but was significantly less than FV1, as shown in Figure 8c. FV5–8 were better than FV1 but still had significant porosity. These results are summarized in Table 7 and compared with measurements from an EOS GmbH sample, which exhibited much lower porosity.

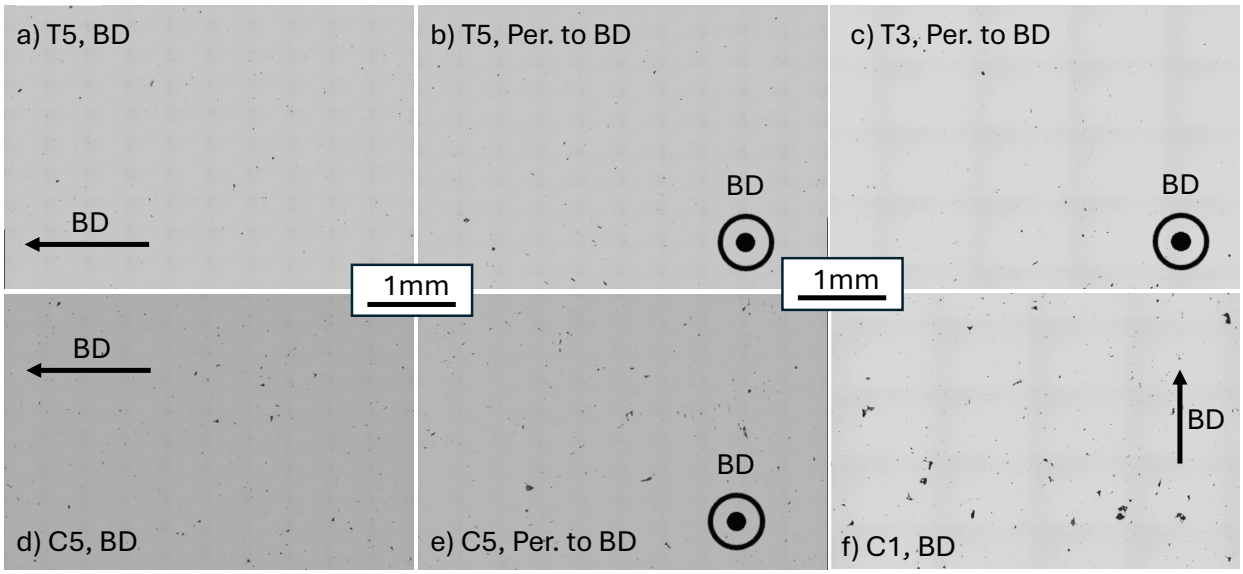

Figure 7. ORNL optical micrographs of the LPBF 282 alloy after heat treatment: (a) T5 specimen along the BD, (b) T5 specimen perpendicular to the BD, (c) C5 specimen along the BD, and (d) C5 specimen perpendicular to the BD.

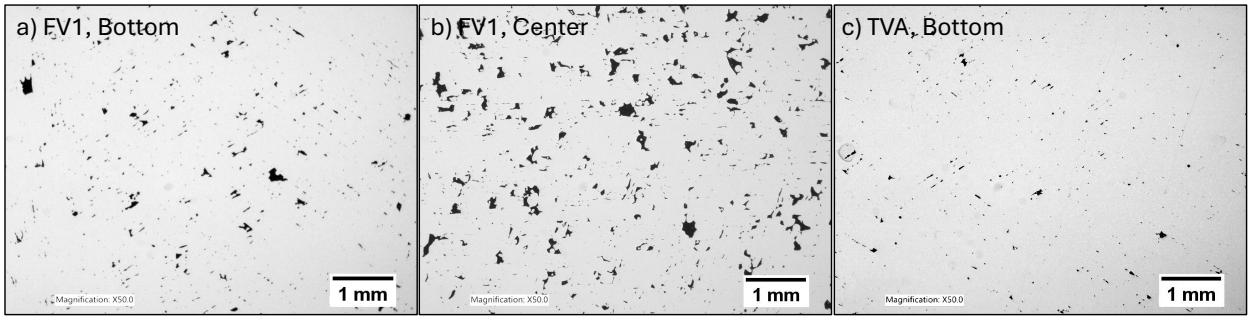

Figure 8. INL optical micrographs of the LPBF 282 perpendicular to the BD: (a) FV1 specimen bottom after heat treatment, (b) FV1 specimen center, and (c) TVA4 specimen bottom.

Table 7. Porosity measurements at INL for several LPBF 282 rods

Sample	Porosity (area %)
TV4, 4 mm end	0.67
FV1, slice 6, bottom	1.95
FV1, center slice	4.76
FV5, bottom	0.79
FV6, top	0.59
FV7, bottom	0.27
FV8, top	1.07
EOS 1100 1 h	0.05

3.1.2.2 Scanning electron microscopy and electron backscatter diffraction mapping

The grain structure of the LPBF 282 alloy was extensively studied; the goal of the 1 h 1,180°C heat treatment was to ensure grain recrystallization while limiting grain growth [8]. To investigate the effectiveness of the heat treatments in recrystallizing the microstructure through thickness, a piece of sample FV1 was reheated to 1,180°C for 1 h and then air-cooled. Scans were taken from the center of the cross section in three different locations. For the INL analysis, the grain size reported is the area-weighted average grain size, since larger grains tend to affect certain mechanical properties more than smaller grains. The twin boundaries were excluded from the analysis due to their unique behavior with regard to dislocation interaction. A misorientation angle of 5 degrees was used to define grain boundaries. Figure 9a shows an inverse pole figure (IPF) map of the centermost location. At the magnification of the scan, avoiding the copious porosity was not possible, so several pores are visible. The map reveals mostly equiaxed grains, indicating that the sample was mostly recrystallized even in the center. Some nonrecrystallized regions are still present. Regions of small grains were found next to the large pores. These regions are present in several of the scans, such as the scan shown in Figure 9b. The scan suggests that either the regions near the pores recrystallized later than the interior regions or grain size was restricted near the pores for another reason.

During the EOS sample heat treatment study performed at INL, the grain growth appeared to occur rapidly after recrystallization, as shown by the difference in recrystallization state between specimens annealed at 1,180°C for 0.5 h vs. 1,180°C for 1 h. Samples annealed at 1,180°C for 0.5 h were mostly unrecrystallized (as shown in Figure 9d), and samples annealed at 1,180°C for 1 h were mostly recrystallized with a grain size of 112 μm (Figure 9c). The microstructure was quite sensitive to time at 1,180°C. This sensitivity explains the difference observed in the slower furnace-cool versus air-cool after heat treatment, as described in this section.

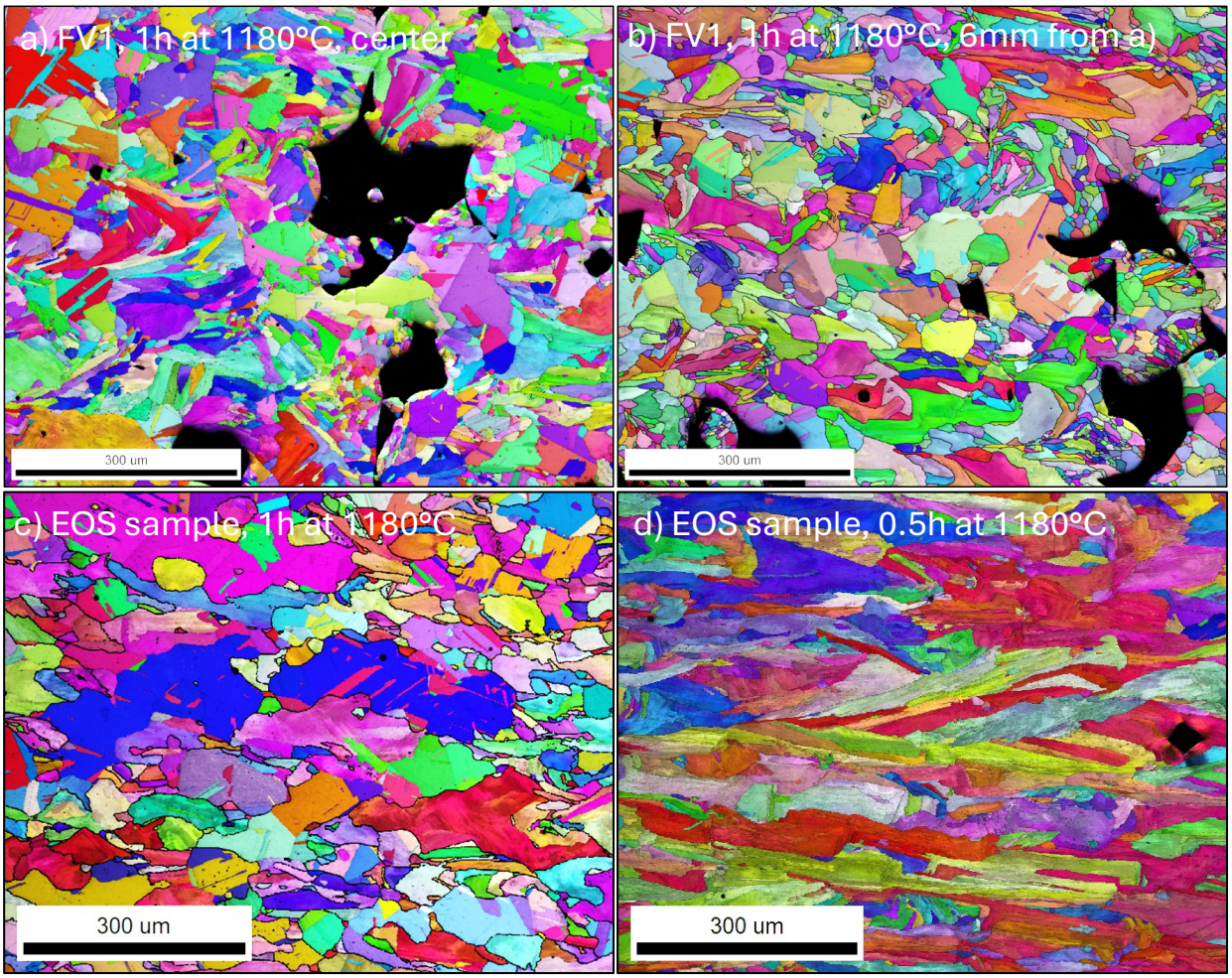

Figure 9. Electron backscatter diffraction IPF map of LPBF 282: (a) center of the FV1 specimen, 1 h at 1,180°C; (b) FV1 specimen, 6 mm away in the radial direction from (a); (c) EOS sample after 1 h at 1,180°C; and (d) EOS sample after 0.5 h at 1,180°C.

When aging the remainder of the tensile and fatigue samples, a mistake in the programming of the furnace was made. The samples were consequently subjected to 1,180°C for 1 min, followed by forced air-cooling. When this was realized, the samples were again reheated to 1,180°C and held for 1 h, followed by air-cooling. The grain size of the sample TV1 was studied to understand the implication of the mistake. Figure 10 shows an IPF map from an electron backscatter diffraction (EBSD) scan from the center of TV1. As seen in Figure 10 and Table 8, the grain size of TV1 after the deviant heat treatment was 141 µm, which is larger than that of FV1 and also slightly larger than the EOS sample that was aged at 1,180°C for 1 h and furnace-cooled. This result indicates that the time that TV1 spent at a temperature close to the critical recrystallization temperature (most likely during the double heat-up) was more similar to the EOS sample time (which included heat-up and furnace-cooling) than FV1, which had a single heat-up and then rapid air-cooling. The recrystallization had enough time to initiate during each heat-up phase of the double heat treatment even though the sample only spent 1 min at 1,180°C for the first heat treatment. It is also interesting that the grain size of sample TV1 in the transverse direction was 108 µm, which indicates an isotropic grain size that was probably a remnant of the initial highly anisotropic microstructure. The grain size of creep sample CV3 was also checked. This sample received a heat treatment of 1,180°C for 1 h followed by air-cooling. The grain size in this case was 77 µm, which was close to that of FV1. The sample that received the double heat treatment at 1,180°C was then aged at

800°C for 4 h to precipitate γ′. The grain size was again checked by EBSD and was 143 μm, which was essentially the same as the solution-treated sample. This result was expected because of the low temperature and because γ′ and carbide precipitation at 800°C should pin the grain boundaries and prevent any significant grain growth. These results are shown in Table 8.

Table 8. Average grain size of LPBF Haynes 282 samples under various aging conditions

Manufacturer	Sample	Condition	Area-weighted average grain size (μm)
EOS	—	as printed	88
	—	1,250°C, 1 h	255
	—	1,250°C, 2 h	282
	—	1,210°C 2 h	327
	—	1,180°C 1 h	112
	—	1,180°C 0.5 h	Mostly unrecrystallized
	—	1,160°C 1 h	Mostly unrecrystallized
ORNL	FV1	1,180°C 1 h	55
	TV1	1,180°C, 1 min + 1 h	141 in BD, 108 in transverse direction
	TV1	1,180°C, 1 min + 1 h + 800°C, 4 h	143
	CV3	1,180°C, 1 h	77

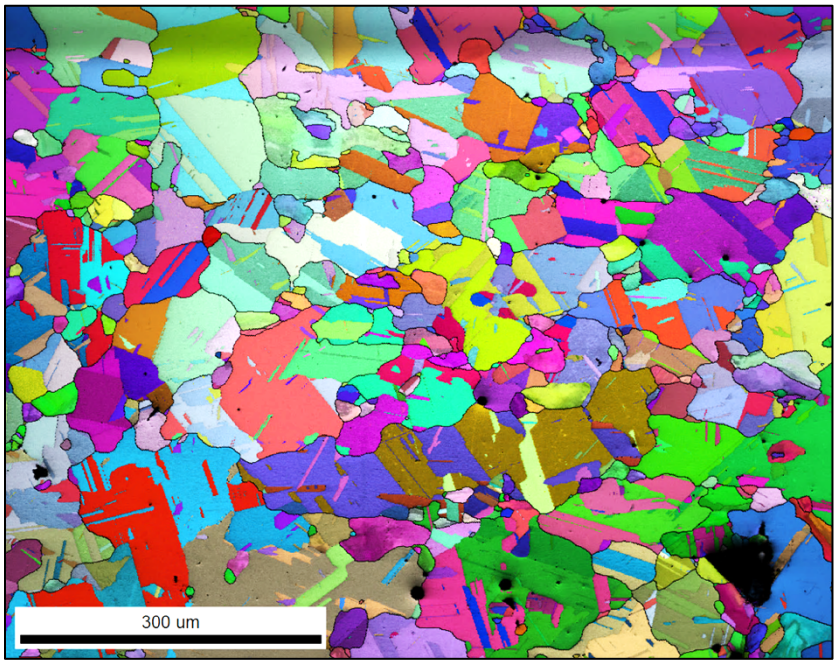

Figure 10. EBSD IPF map of LPBF 282 at the center of TV1 after double heat-up at 1 h and 1,180°C.

Similar grain structure characterization was conducted at ORNL, and EBSD IPF maps for the C1 and T3 specimens annealed for 1 h at 1,180°C are presented in Figure 11. As previously described, partial recrystallization was achieved with multiple areas of small grains leading to an average equivalent diameter of approximately 15 μm. However, the average grain size numbers were highly dependent on

the methodology to calculate the grain size from EBSD data. Figure 11b and Figure 11c highlight the importance of twin boundaries as well as the grain tolerance angle.

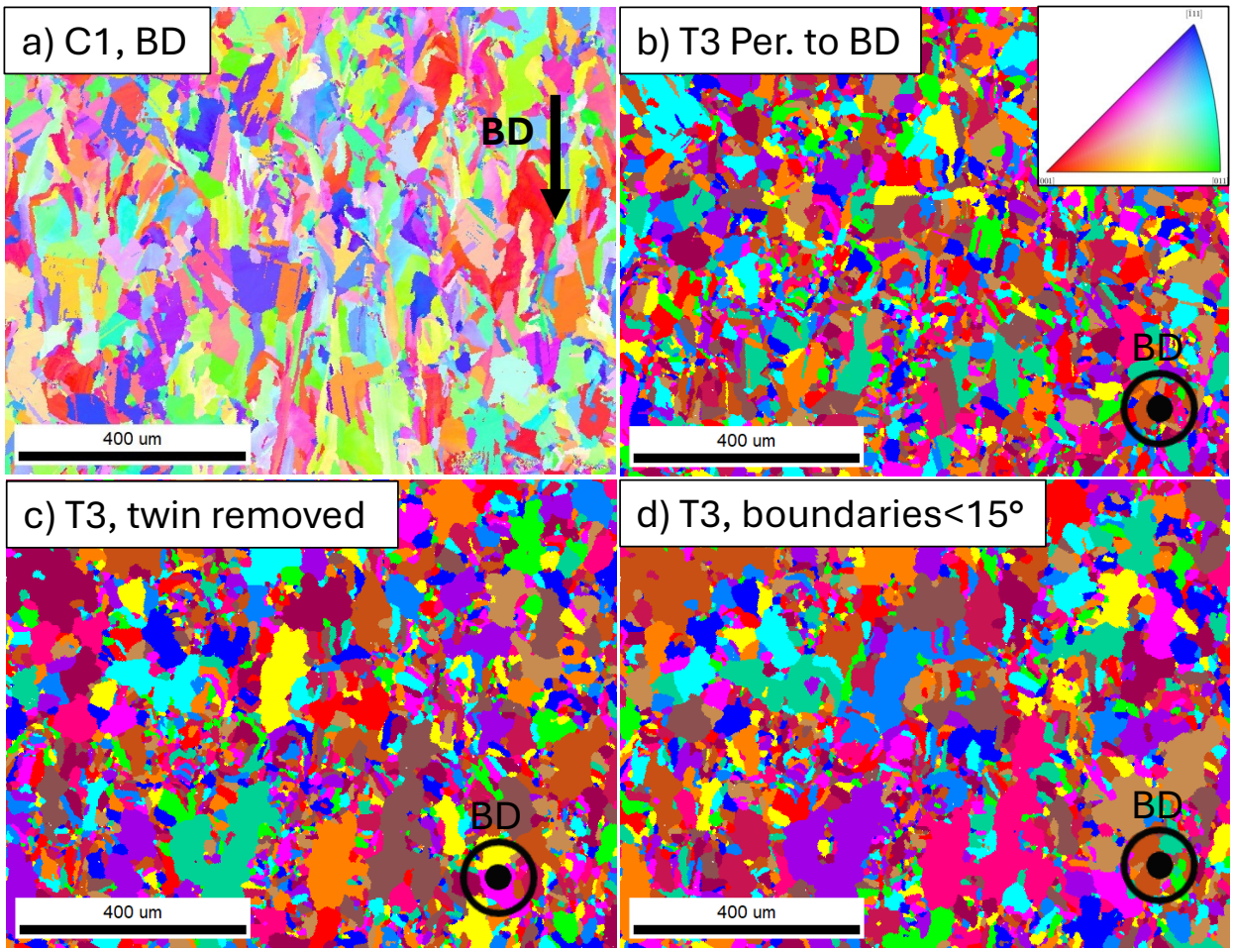

Figure 11. EBSD IPF map of LPBF 282 after 1 h at 1,180°C: (a) C1 specimen along BD, (b–d) T3 specimen perpendicular to BD—(b) all grains, (c) twin boundaries removed, and (d) grain tolerance angle <15°.

3.1.2.3 X-ray computed tomography

Nondestructive analysis was conducted using an Industrial ZEISS METROTOM XCT system equipped with a 200 kV source at ORNL. Radiographic images of the gage section of the creep specimens were captured from various angles and used to algorithmically reconstruct 3D representations of these specimens. For all XCT scans, a short-scan strategy with 145 views between 0° and 197° was employed, and each view had an average acquisition of 8 × 1 s. Reconstruction was performed for XCT scans acquired before and after creep testing using advanced deep learning–based algorithms [28], and the evolution of flaws during creep testing will be discussed later in this report.

XCT was also performed on all creep and cyclic specimens at INL prior to testing, with examples of 2D and 3D visualization shown in Figure 12. For each example, three cross-sectional images are shown—two taken longitudinally, one circumferentially, and one “through thickness” to demonstrate the flaw density through a volume of the specimen. Although these images do not show the entirety of the data collected during the XCT scan, they do provide a representative example of the structure of the specimens. Of the creep specimens, TV-1 had significant defects, CV-4 and CV-5 had relatively few defects, and the rest

were in between with some moderate level of defects. FV-2, FV-3, and FV-4 had a noticeably higher void density than the other fatigue specimens. Additional XCT images can be found elsewhere [27].

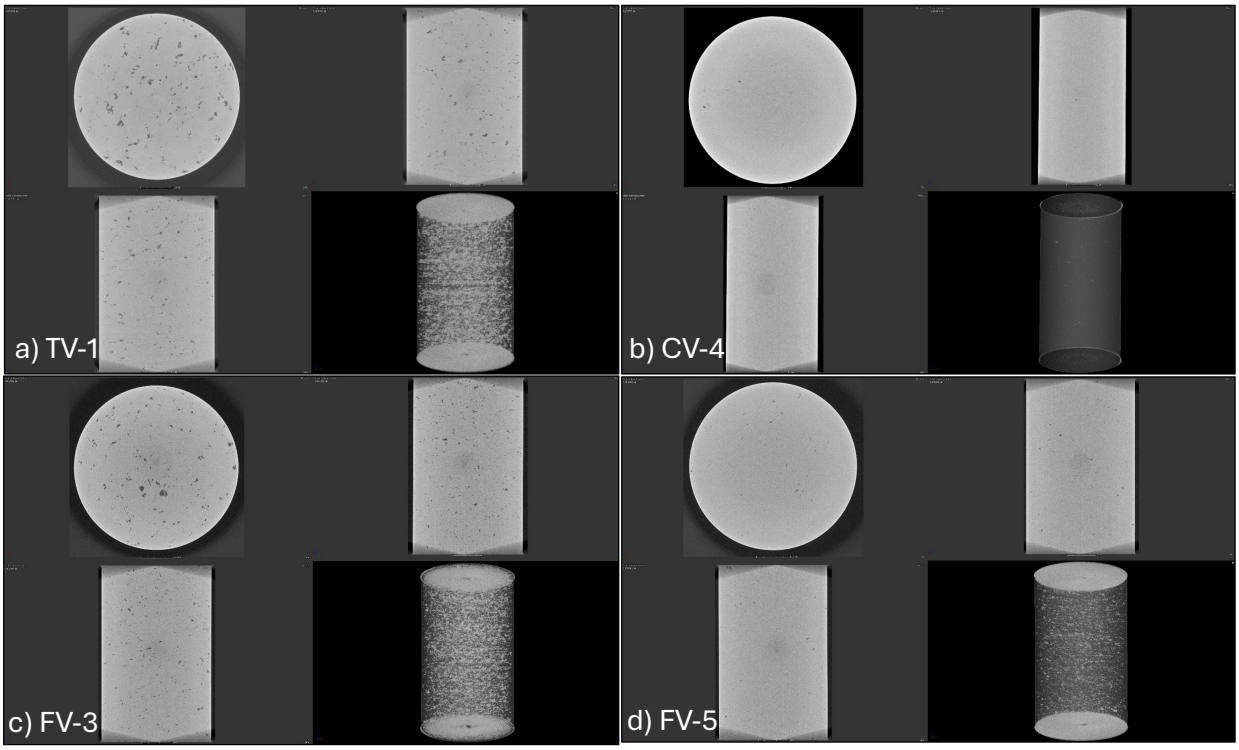

Figure 12. Example of cross sections and full-volume section from the XCT scans of specimens (a) TV-1, (b) CV-4, (c) FV-3, and (d) FV-5.

3.1.3 Creep Testing

3.1.3.1 Creep curves

As described in Table 6, six creep tests were conducted at 750°C at ORNL, and four creep tests were conducted at INL at the same temperature. Creep testing at ORNL was conducted with an applied stress of 300 or 350 MPa using lever arm machines according to ASTM Standard E139 [29]. Thermocouples were attached to the gage section, and the temperature was maintained at 750°C ± 3°C. Rods clamped to the specimen heads were connected to linear variable differential transformers to measure specimen deformation. Creep testing was also conducted at 300 and 350 MPa to compare with the ORNL results, and testing at 320 MPa was carried out to compare with previous data generated on wrought Haynes 282 as part of a concentrating solar power program that was examining potential receiver materials, including Haynes 282 [30].

The creep curves presented in Figure 13 revealed similar secondary creep rates but lower ductility and slightly lower lifetimes for the C1 and C3 specimens compared with the T1 and T3 specimens. The C5 and T5 curves were very similar, and the tests were interrupted for XCT scan analysis before rupture. Higher creep rates were measured for the specimens tested at INL, but the lifetimes were similar except for the TV1 specimen, which was tested at 350 MPa, that ruptured abruptly after only 33 h. The strain at rupture for all the LPBF 282 specimens was quite low; the wrought 282 ductility was expected to be >20% at 750°C [19]. Direct comparison of the creep performance of the LPBF 282 and wrought 282 is highlighted in Figure 14 with creep curves at 750°C with an applied stress of 320 MPa. A drastic decrease

in creep properties was observed for the LPBF 282 specimen with a rupture life of 220 h compared with lifetimes around 1,400 h for the wrought 282 specimens. Final elongation was determined at INL by measuring the specimens directly after testing, and the results are summarized in Table 9.

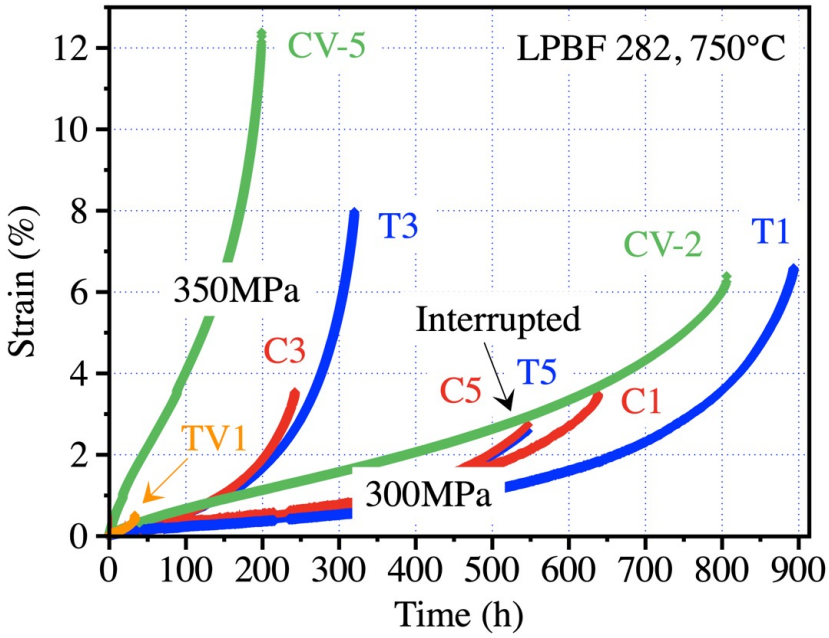

Figure 13. LPBF 282 creep curves generated at 750°C with an applied stress of 300 or 350 MPa at ORNL and INL.

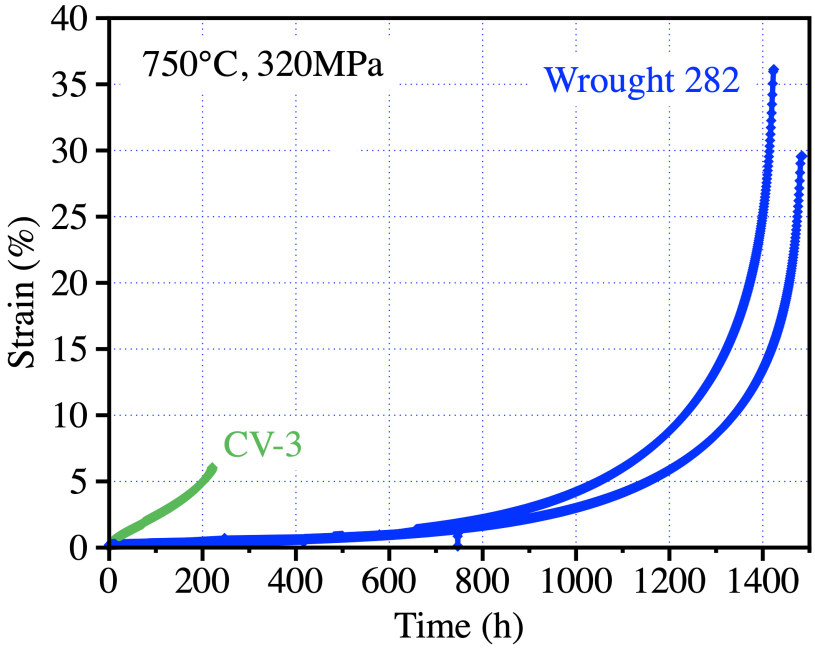

Figure 14. LPBF 282 and wrought 282 creep curves generated at 750°C with an applied stress of 320 MPa at INL.

Table 9. Summary of the rupture time and elongation for the INL creep specimens

Specimen	Temperature (°C)	Stress (MPa)	Rupture time (h)	Post-test elongation (%)
CV2	750	300	806	5.97
CV3	750	320	221	5.39
CV5	750	350	199	11.07
TV1	750	350	33	1.89

3.1.3.2 Microstructure analysis of the LPBF 282 creep specimens

The 3D reconstructions shown in Figure 15a and Figure 15b from the XCT scans of the C3 and T3 specimens before and after testing confirmed the significantly higher volume fraction of flaws in the C3 specimen compared with the T3. Additionally, an increase in flaws after testing was obvious for both the C3 and T3 specimens. The volume fractions of flaws before and after testing were estimated from the XCT scans and are given in Figure 15c. In addition to the expected difference between the C and T specimens, significant variation was also observed between the C1, C3, and C5 specimens. An increase in flaws after creep testing was confirmed for all the LPBF 282 specimens, and additional analysis of the flaw distribution in the specimens before and after testing is given in Figure 16.

For the T1, T3, and T5 specimens, a significant increase of the number of flaws less than 250 μm in size was observed after creep testing. These new flaws are likely related to creep cavitation, and cross-sectional microstructure characterization will be performed to determine if these flaws are related to specific microstructural features. An increase in size of a few very large flaws was observed for T1 and T3, which were tested to rupture, but this increase was not found for the interrupted T5 specimen. These flaws likely play a key role in the final rupture stage of the specimens and might partly explain the LPBF 282 alloy's low ductility.

The initial number of flaws less than 250 μm in size was drastically higher for the C1 and C3 specimens in comparison with the T1 and T3 specimens (Figure 16). A further increase of these flaws of 250 μm or less was observed after creep testing for the C3 specimen and to a lesser extent for the C1 specimen. For the later specimen, however, creep testing resulted in a drastic increase of the number of flaws more than 250 μm in size. Ongoing work is aiming at the registration of each initial flaw for all the specimens to determine which and how flaws are affecting specimen failure. Microstructure characterization of the creep specimens is also ongoing, and Figure 17 shows optical mosaics over the entire width of the C3 specimens before and after etching. A Python code is being developed to rapidly analyze these optical micrographs and compare flaw volume fractions with the volume fractions estimated from the XCT scans. The code will also identify the type of flaws (i.e. lack of fusion, key hole, or creep cavity) based on the flaw geometry. Analysis of a large image dataset will allow researchers to establish a correlation between these flaws and microstructure features such as grain boundaries. While less analysis has been performed on the XCT scans, a moderate defect density was observed in the CV-3 specimen prior to creep testing, as seen in Figure 18.

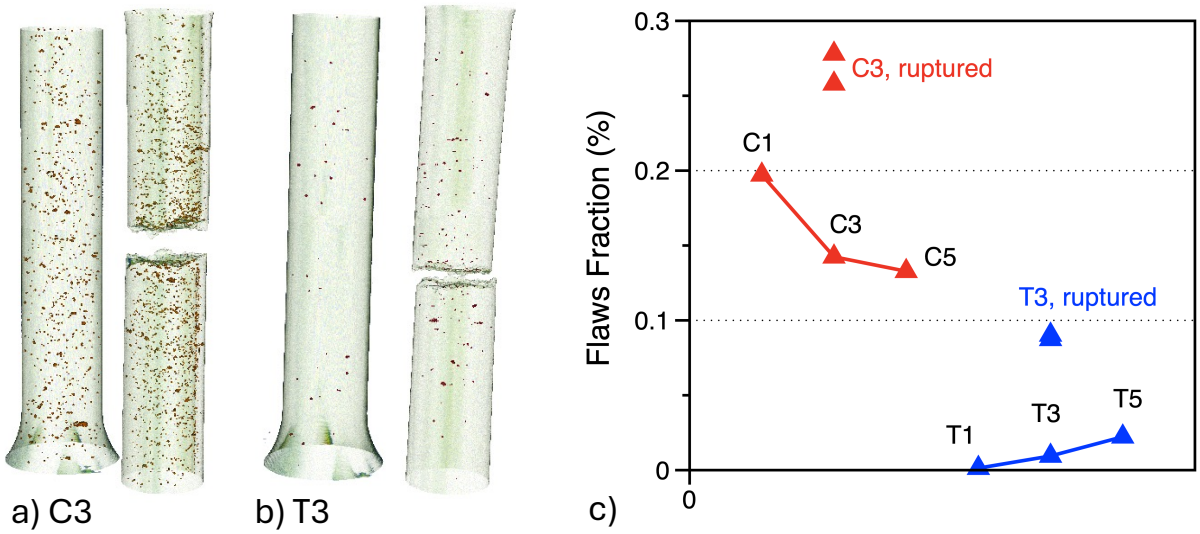

Figure 15. 3D reconstruction of the (a) C3 and (b) T3 specimens before and after creep testing. (c) Volume fraction of flaws in the C and T specimens before and after creep testing.

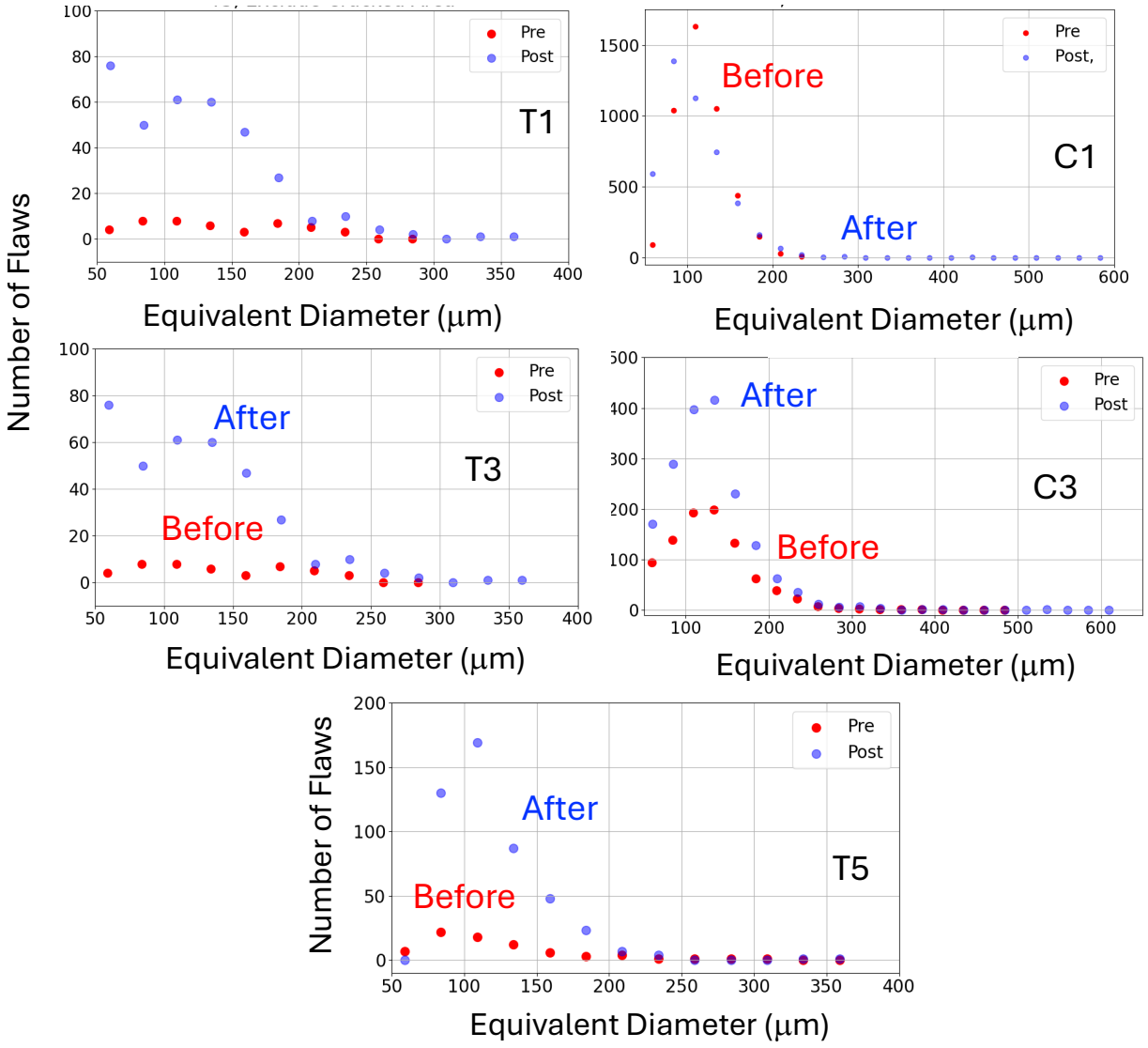

Figure 16. Number of flaws versus equivalent diameter for all the LPBF 282 specimens before and after creep testing. The rupture area was removed because a flaw's size was difficult to evaluate.

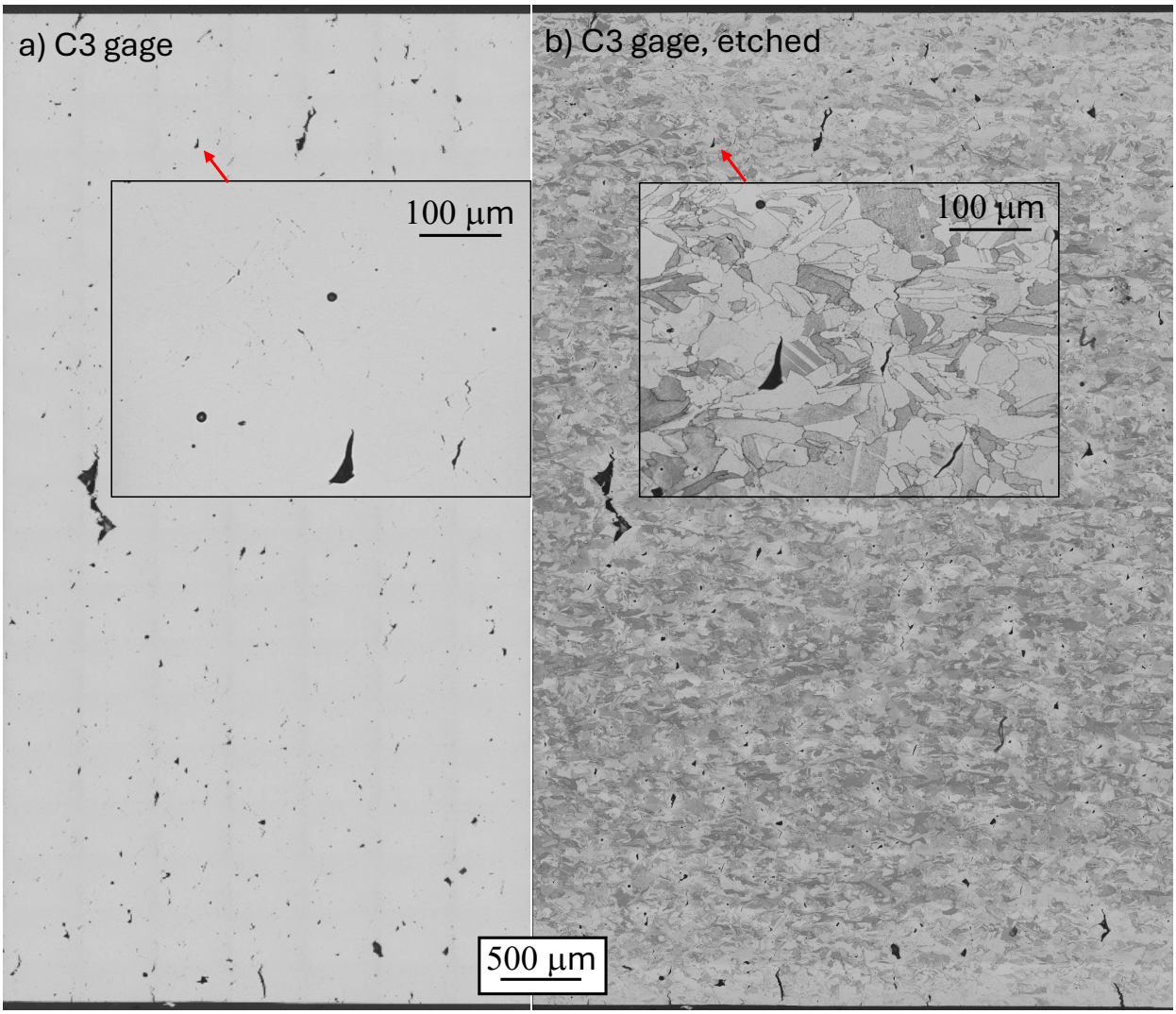

Figure 17. Optical mosaics of the C3 specimen after creep testing at 750°C and 350 MPa (a) before etching and (b) after etching. Inserts show one individual micrograph.

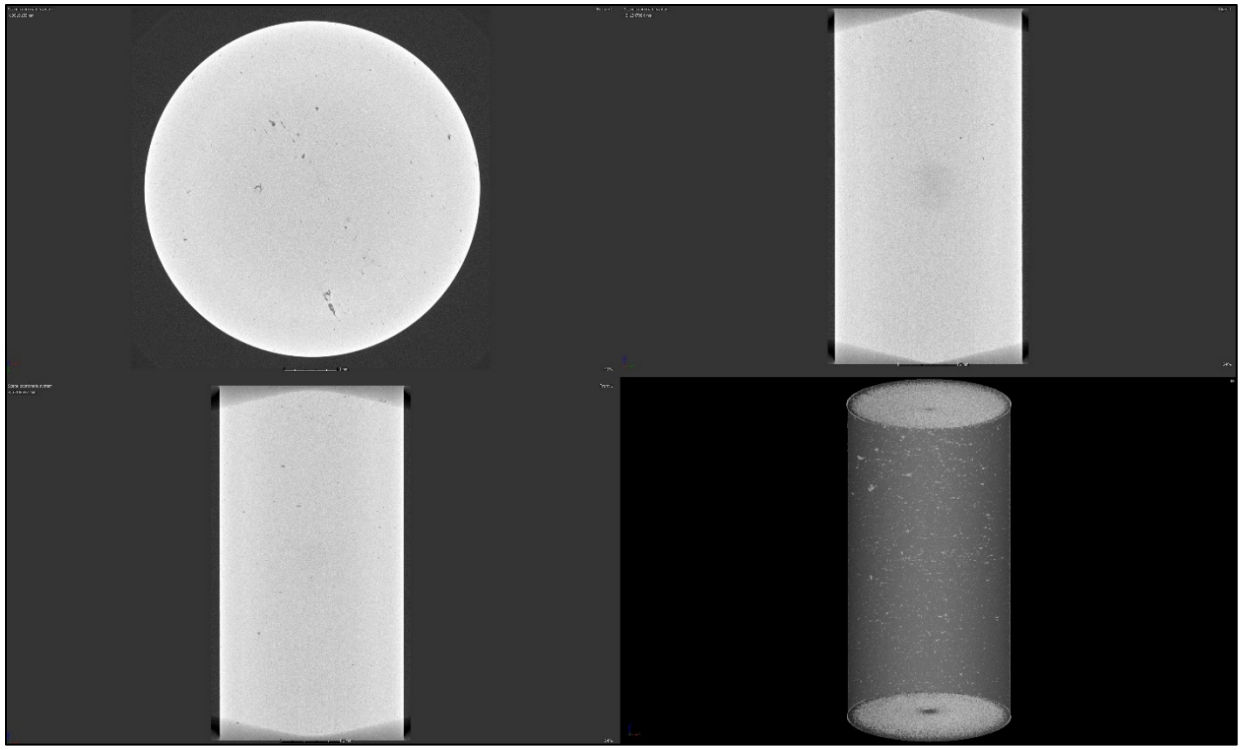

Figure 18. Moderate flaws density observed in CF-3 by XCT scans prior to creep testing.

3.1.4 Cyclic Testing

Fatigue and a creep-fatigue tests were performed on the LPBF material at conditions that could be compared with the wrought material tested in the solar program [30]. Creep-fatigue is a cyclic test similar to fatigue with the inclusion of a hold time each cycle at peak strain. In this case, the hold time was 10 min, during which time stress relaxation is allowed to occur. Typically, a significant decrease in cyclic life is observed in creep-fatigue tests as compared with fatigue because of the interaction between creep and fatigue damage. The results shown in Figure 19 show that the LPBF material, similar to the creep testing, has poorer life when compared with the wrought material for both fatigue and creep-fatigue. It should be noted that the LPBF 282 tested had a high level of initial defects, as seen in Figure 20 and Figure 21.

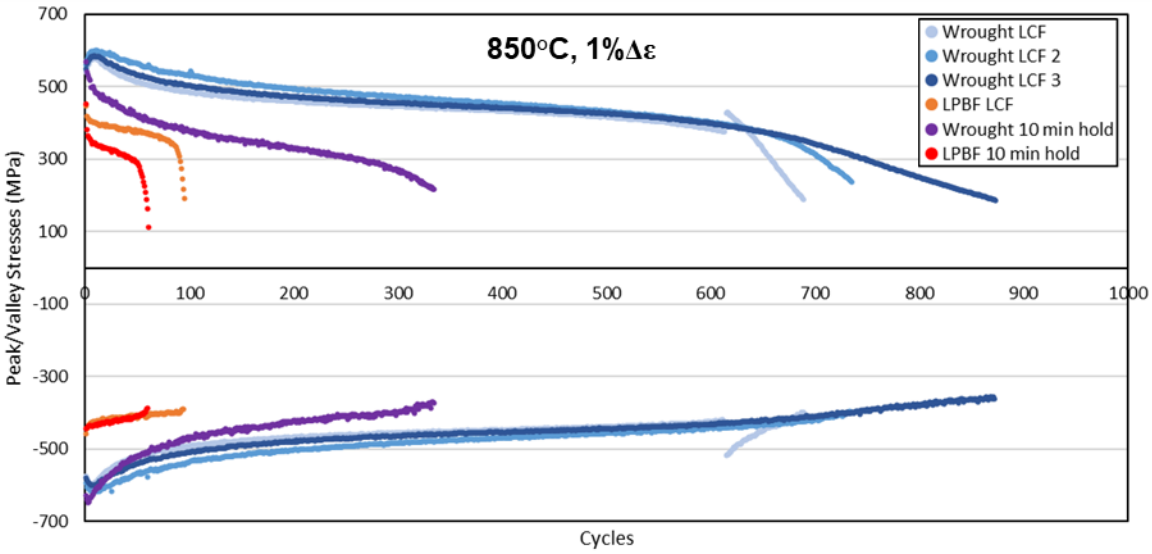

Figure 19. Fatigue curves of LPBF Haynes 282 tested in this program compared with wrought material tested as part of a concentrating solar power project [30].

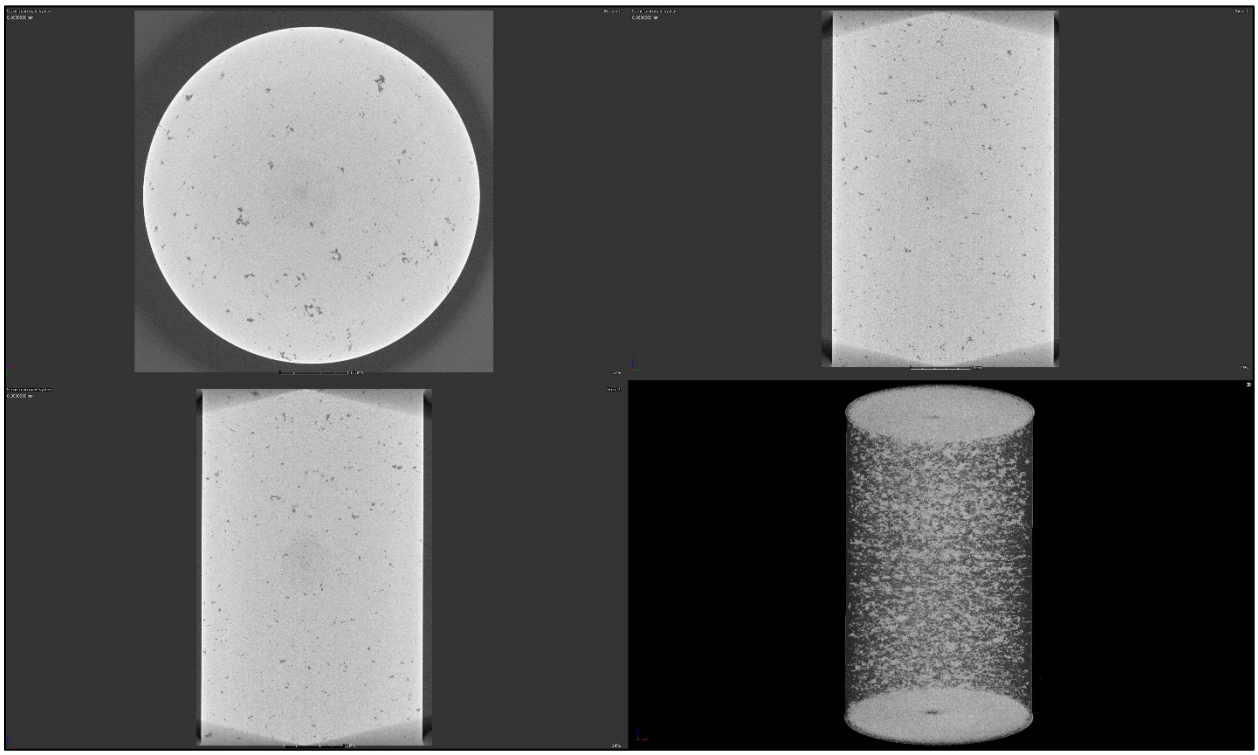

Figure 20. Specimen flaws observed by XCT prior to creep-fatigue testing.

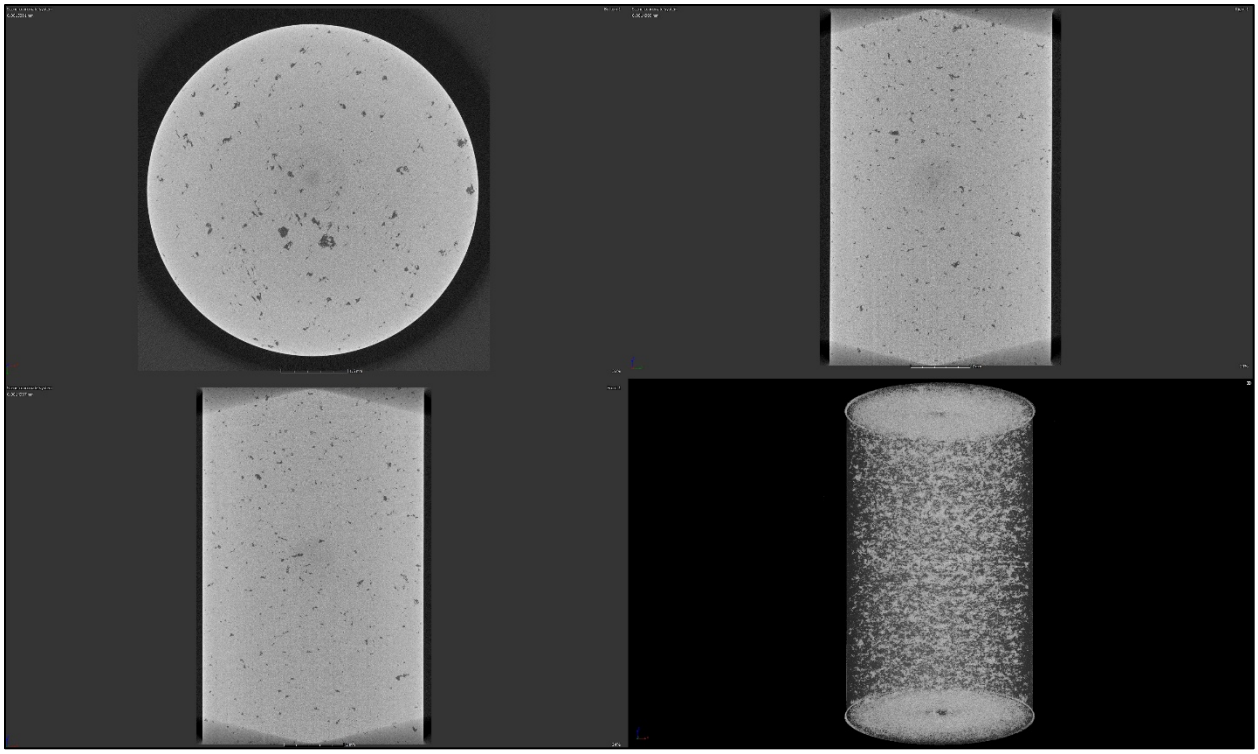

Figure 21. Specimen flaws observed by XCT prior to fatigue testing.

3.2 LASER POWDER DIRECTED ENERGY DEPOSITION

LP-DED is an AM process developed for a wide range of applications. LP-DED is a solid freeform manufacturing technique that transforms metallic powders into dense 3D parts from a CAD model, following the process described in Figure 22.

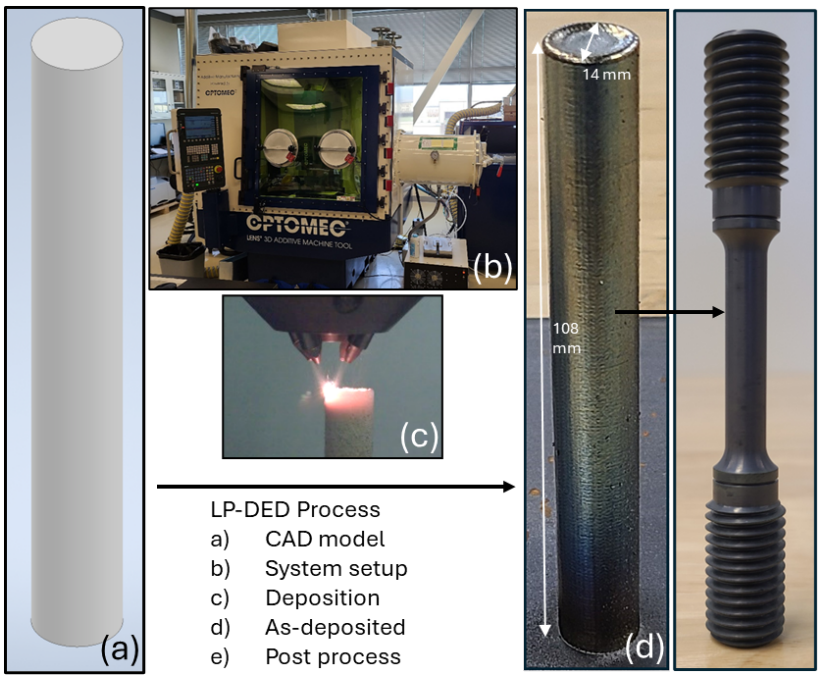

Figure 22. LP-DED process flow. (a) Part is developed as a CAD model; (b) the model is sliced, and G-code/M-code is created; (c) part is fabricated using blown powder deposition; and (d) the as-deposited part then goes into (e) postprocessing involving heat treatment and machining.

Commercially supplied, gas-atomized HY282 powder was used for this work. The powder has a composition as shown in Table 5, which was measured by optical emission spectroscopy with a particle size distribution of 45–105 µm in diameter. The substrate was a 6 × 6 × 0.5 in. 1020 steel plate. During the LP-DED process, key parameters, including laser power, powder feed rate, and deposition rate, influenced the final microstructure and mechanical properties. These parameters were selected based on initial test prints to reduce the number of voids. The process parameters, laser power (300 W), powder feed rate (9.5 g/min), deposition rate (9.3 mm/s), hatch spacing (0.381 mm), hatch angle (67°), and layer thickness (0.127 mm) were used to fabricate cylinders with dimensions of 108 × 14 mm.

The system used in this work at INL was an Optomec MTS 500, which uses a laser to melt metallic powder fed through four nozzles toward the focal plane of the laser beam. The system uses a 1,070 nm wavelength and a 1 kW YLR laser from IPG Photonics with a focused beam diameter of 0.6 mm. The samples were deposited in an Ar environment by evacuating to a pressure of 4.5 Torr and backfilling with 99.9% purity Ar. More Ar gas with the same purity was also used as a shielding gas and the powder carrier gas. Hardness measurements were taken on the as-deposited, solution-annealed, and aged material. The final hardness values were calculated by averaging the 80 indentations arranged in an 8 × 10 matrix with spacing of 500 µm.

3.2.1 Powder Feedstock

Scanning electron microscopy (SEM) images, shown in Figure 23, of HY282 powder feedstock show a nonuniform powder morphology with the presence of nonspherical and amorphous particles. For LP-DED, spherical powder with a size distribution of 45–150 µm is ideal to limit the formation of interlayer porosity. The nonuniform sphericity of the powder increases the chance that interlayer porosity will develop in the LP-DED specimens. The chemical composition analysis for the as-deposited material is shown in Table 5. No significant changes were noted in the elements measured. However, influential elements such as C, O, N, and B have not been measured but are critical for future analysis.

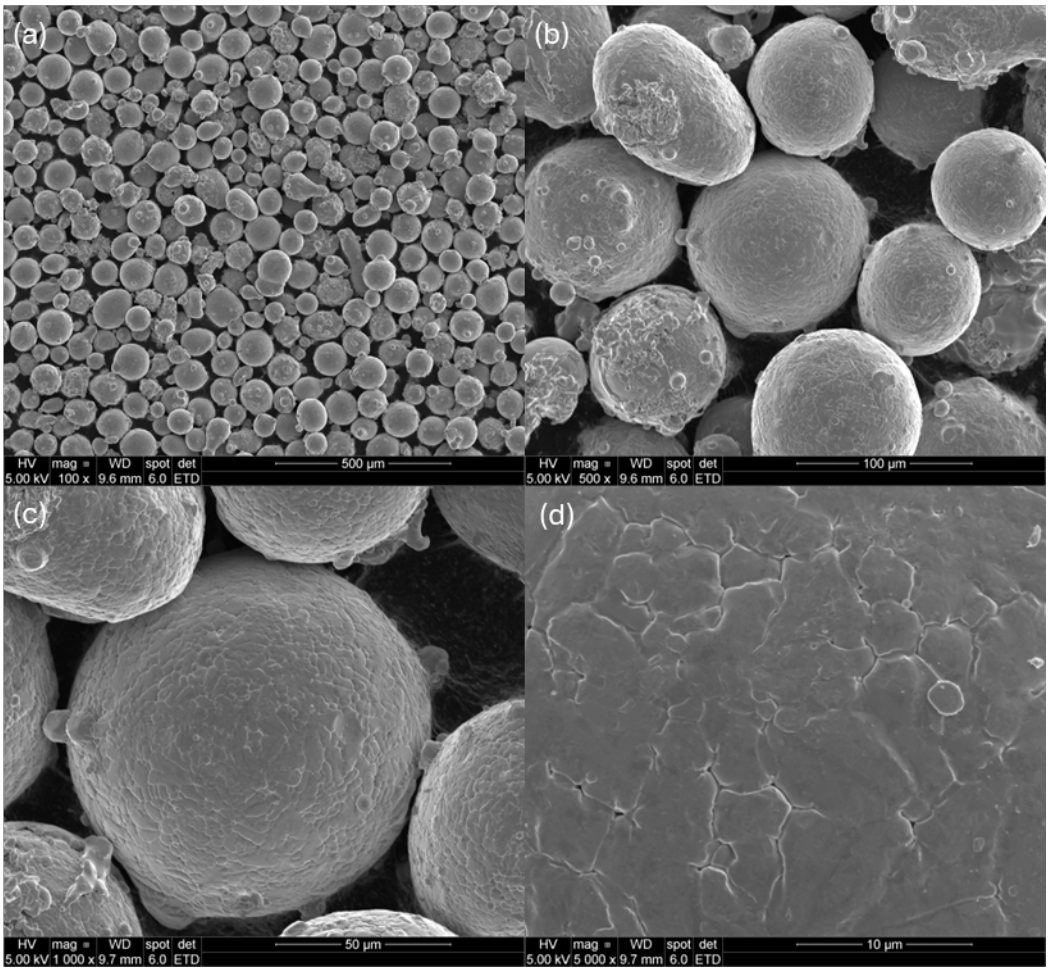

Figure 23. SEM electron backscatter image showing morphology and particle size distribution of Haynes 282 powder feedstock for LP-DED at (a) 100×, (b) 500×, (c) 1,000×, and (d) 5,000×.

3.2.2 EBSD Analysis

EBSD analysis was performed on the as-deposited, solution-annealed, and age-hardened conditions as shown in Figure 24 and Figure 25. The as-deposited sample, which appears in the top images in Figure 24 and Figure 25, showed epitaxial grain growth oriented toward the [111] direction, although the number of grain samples is very limited at this point. After annealing at 1,180°C for 1 h, shown in the center image in Figure 24 and Figure 25, incomplete recrystallization was observed with elongated columnar grains associated with solidification in metal AM processes mixed with equiaxed grains. Annealing twins were also seen in the material, which are known to form during recrystallization in low-stacking fault energy materials such as Ni-based alloys [31]. Scans after the age hardening at 800°C for 4 h are shown in the lower images in Figure 24 and Figure 25.

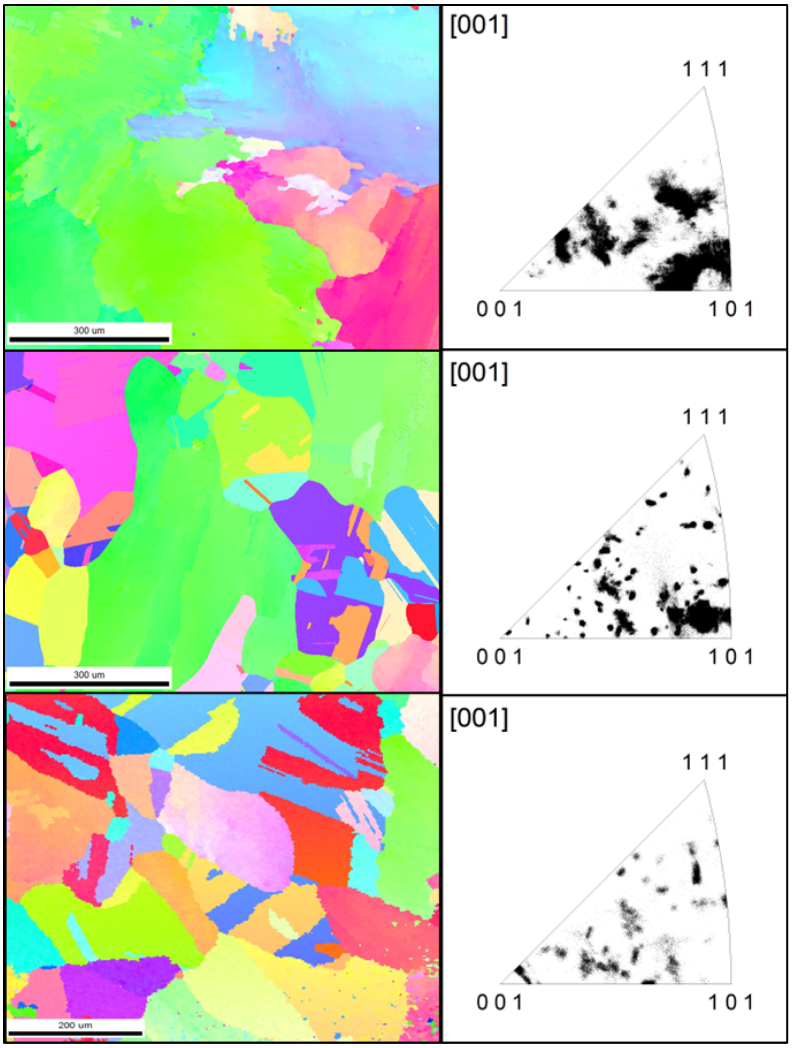

Figure 24. EBSD analysis normal to the build direction of HY282 fabricated by LP-DED in (top) as-deposited, (center) solution-annealed, and (bottom) age-hardened conditions.

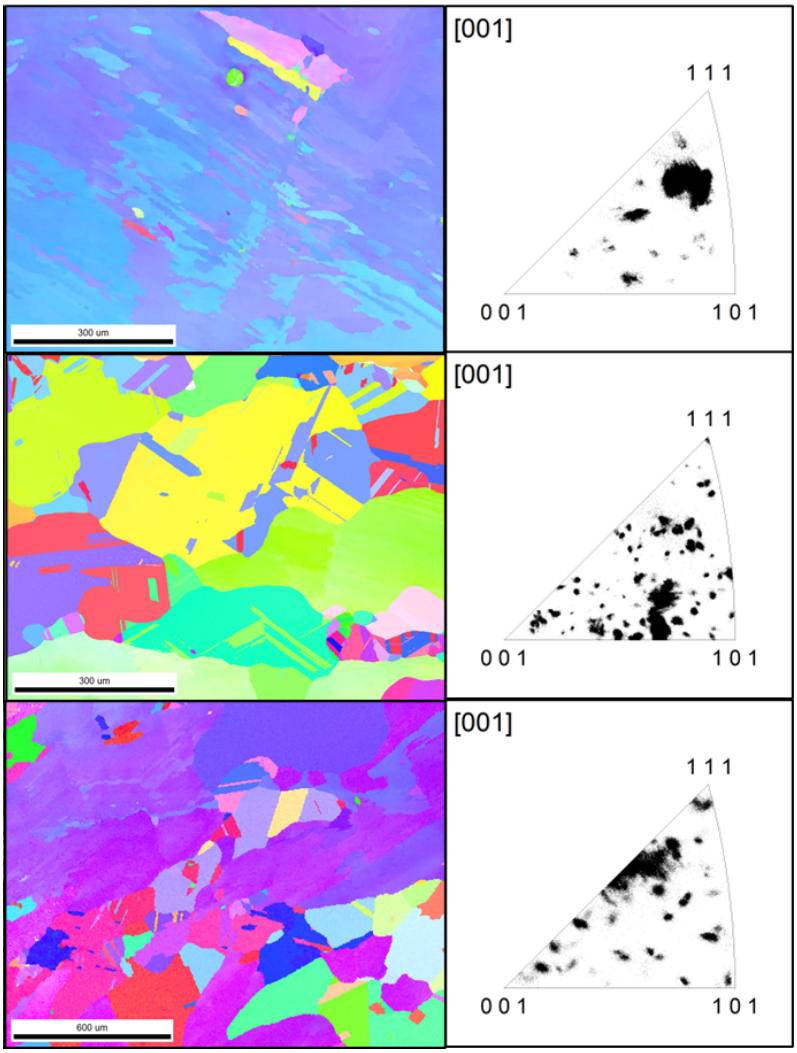

Figure 25. EBSD analysis transverse to the BD of HY282 fabricated by LP-DED in (top) as-deposited, (center) solution-annealed, and (bottom) age-hardened conditions.

3.2.3 Carbide Evolution

SEM and energy-dispersive x-ray spectroscopy (EDS) analysis, provided in Figure 26, showed concentrations of Ti and Mo dispersed through the metal matrix, indicating the presence of (Ti, Mo)C carbides in the as-deposited and annealed samples. The age-hardened sample showed concentrations of Mo, Mn, and Cr along the grain boundaries, suggesting the presence of $(Cr, Mn, Mo)_{23}C_6$ carbides with (Ti, Mo)C carbides still present, as shown in Figure 27. Cast HY282 showed similar trends for carbide evolution during heat treatment [32].

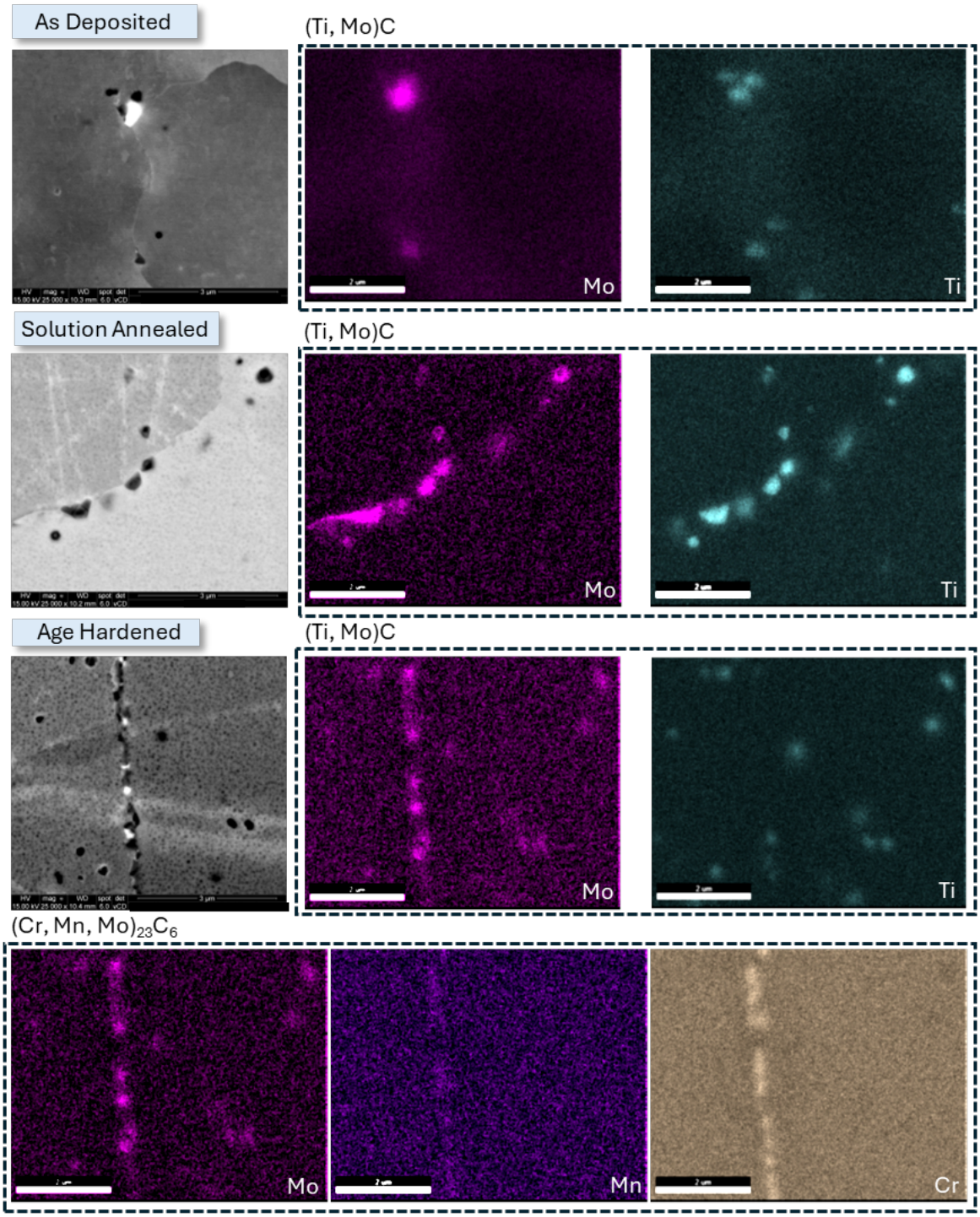

Figure 26. SEM and EDS analysis of the evolution of (Ti, Mo)C and (Cr, Mn, Mo)$_{23}$C$_6$ carbides during the heat treatment process. Only (Ti, Mo)C is present in the as-deposited and annealed materials.

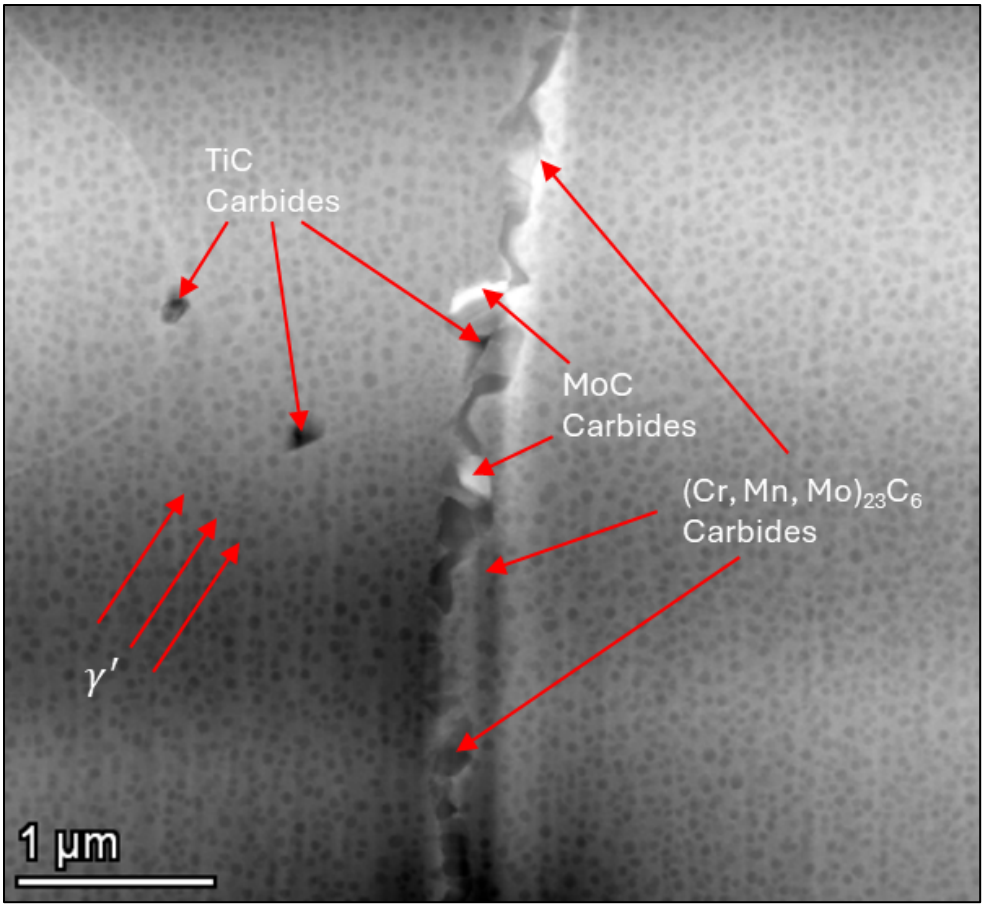

Figure 27. Transmission electron microscope image showing γ′ precipitation and discrete carbides along the grain boundary and distributed throughout the metal matrix in an age-hardened LP-DED HY282 sample.

3.2.4 Scanning Transmission Electron Microscopy Analysis

Scanning transmission electron microscopy (STEM) line scans across γ′ precipitates, provided in Figure 28, showed an increase in the atomic weight percent of Ni, Al, and Ti with a decrease in Cr and no notable change in Co or Mo. A scan across a grain boundary showed a significant increase in atomic weight percent of Cr with a corresponding decrease in Ni. Additionally, an increase in Mo occurred with a decrease in Al, Co, and Ti. At an approximately 22 nm distance, γ′ precipitates appear to be along the grain boundary with a notable increase in Ni, Al, and Ti and with a decrease in Cr and Mo. A line scan across a secondary carbide showed a significant increase in Ti and decrease in Ni. A slight increase in Mo and decrease in Cr, Co, and Al were also present. STEM EDS, shown in Figure 29, resulted in a map showing the elemental distribution around the grain boundary of the age-hardened HY282 sample fabricated by LP-DED. EDS mapping indicated the presence of $(Cr, Mn, Mo)_{23}C_6$ carbides along the grain boundary and (Ti, Mo)C carbides along the grain boundary as well as distributed throughout the metal matrix.

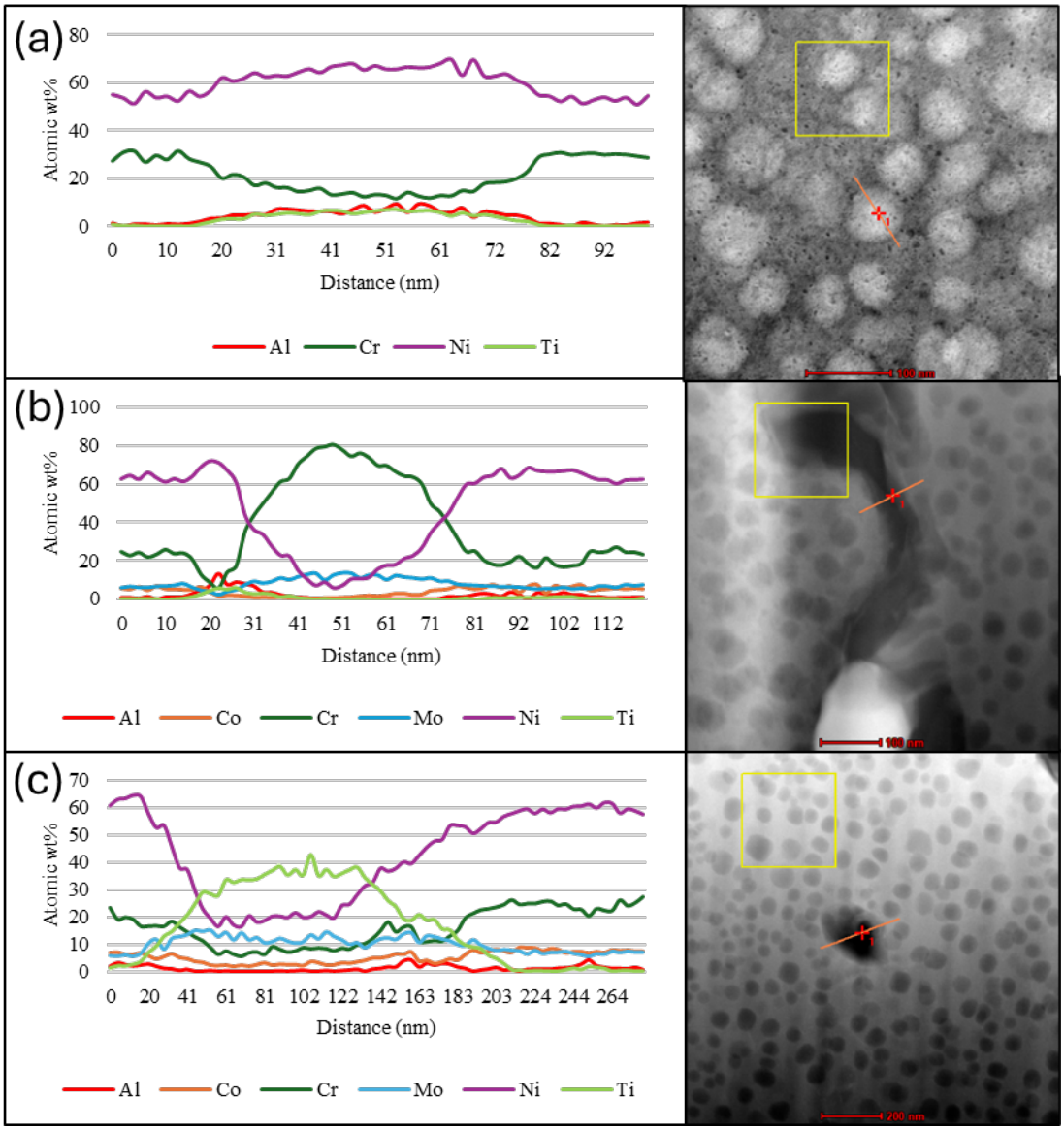

Figure 28. STEM and EDS line scans across (a) γ′ precipitates, (b) grain boundary, and (c) secondary TiC carbide.

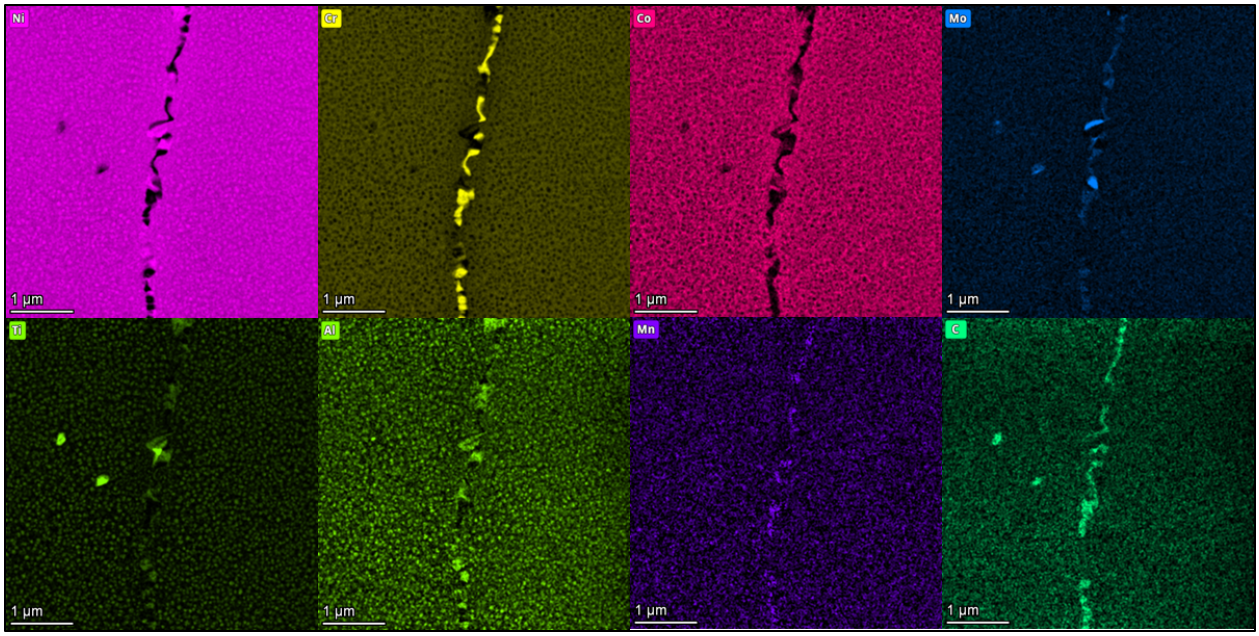

Figure 29. STEM EDS map showing elemental distribution around grain boundary of age-hardened HY282 sample fabricated by LP-DED.

3.2.5 Hardness

The hardness values for LP-DED and GMA-DED are shown in Figure 30. The as-built hardness of the LP-DED was nearly 50 $HV_{0.3}$ (Vickers hardness) greater than the as-built wire DED material. After heat treatments, the hardness values were comparable for both materials within the error of ±1 standard deviation. The age-hardening heat treatment resulted in the highest hardness of nearly 350 $HV_{0.3}$ likely because of the precipitation and finer distribution of γ′. For comparison, the hardness of cast Haynes 282 in the annealed and age-hardened conditions are reported to be 250 and 263 HV, respectively [33]. Hardness levels near 350 HV for aged Haynes 282 in wrought (sheet) form have been observed [34].

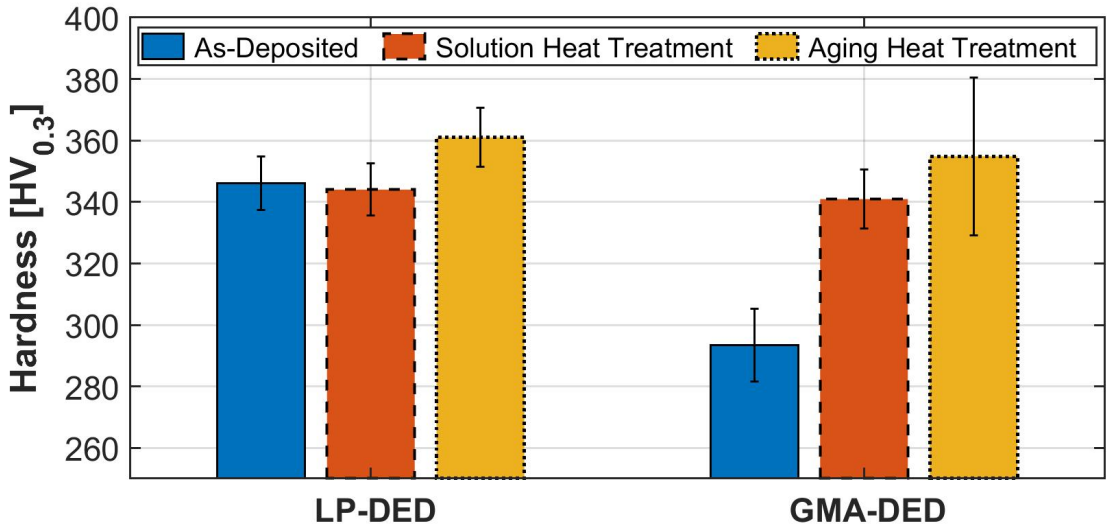

Figure 30. Micro-Vickers hardness for HY282 LP-DED and GMA-DED.

3.2.6 X-Ray Diffraction

The x-ray diffraction (XRD) plots of the powder feedstock, as-deposited, and heat-treated HY282 samples are shown in Figure 31. The diffraction peaks in the specimens corresponding to the γ and γ′ phases occurred at 2θ = 43.5°, 50.7°, 74.6°, 90.6°, and 96°, which correspond to the diffraction of (111), (200), (220), (311), and (222) planes, respectively, of the γ and γ′ phase. Because of the very small lattice parameter variation between γ and γ′, the presence of the γ/γ′ phase was difficult to differentiate in Ni-based superalloys [35]. The metal (M) carbides MC, M_6C, and $M_{23}C_6$ usually have weak intensities because of the very low volume fraction of carbides and their small size. However, peaks corresponding to MC carbides occurred around 2θ = 42°, 77.5°, and 96.7°, with increasing intensity from as-deposited to age-hardened. The peak at 2θ = 54° indicated the presence of the undesirable η phase. The Ni-based superalloys with high Ti/Al ratios commonly show precipitation of the η phase, which has an ordered hexagonal $D0_{24}$ structure with a Ni_3Ti stoichiometry and is the equilibrium phase corresponding to the metastable γ′-Ni_3(Al, Ti) [36].

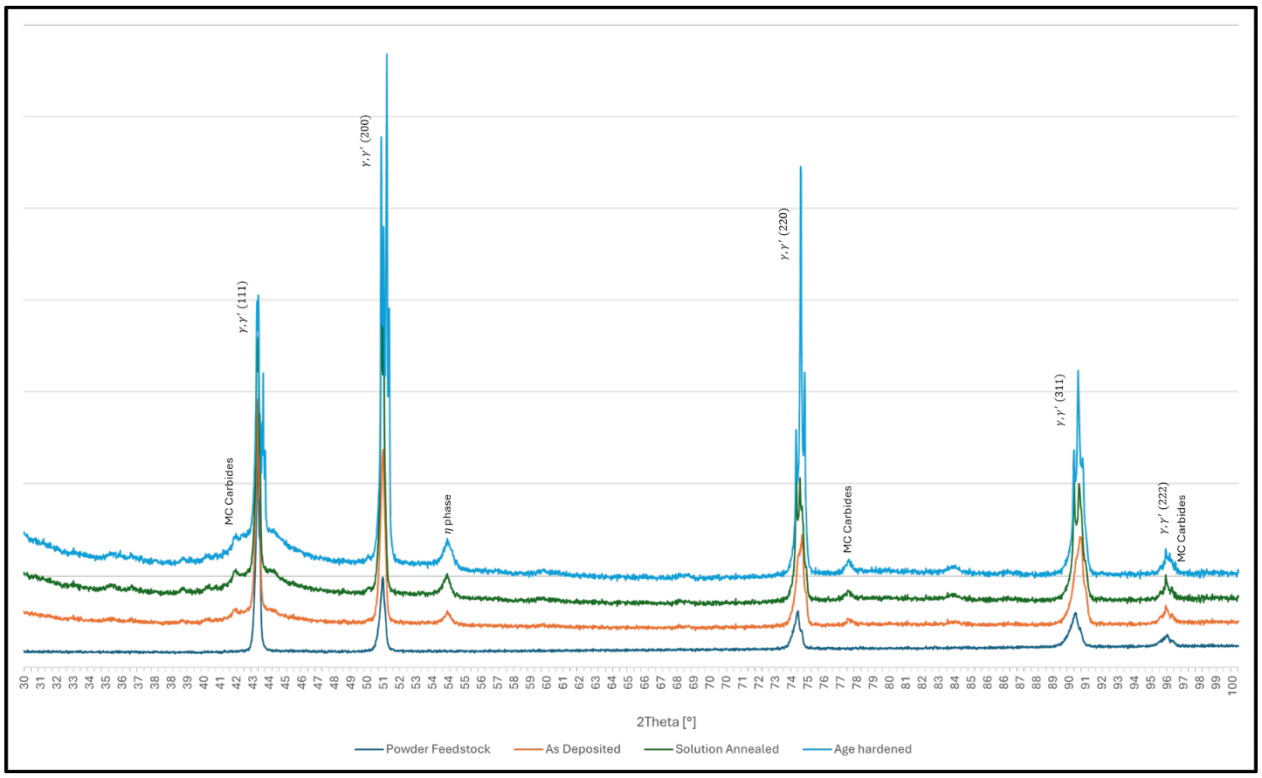

Figure 31. XRD plots of powder, as-deposited, solution-annealed, and age-hardened samples.

3.3 GAS METAL ARC DIRECTED ENERGY DEPOSITION: SCANNING ELECTRON MICROSCOPY ELECTRON DISPERSIVE SPECTROSCOPY ANALYSIS

EDS mapping in GMA-DED HY282, presented in Figure 32 through Figure 34, shows concentrations of Ti and Mo distributed throughout the metal matrix and along grain boundaries. These concentrations indicate the presence of secondary carbides and nitrides. The Laves phase present in the solution-annealed sample (Figure 33) shows similar concentrations. Porosity is also present in the solution-annealed EDS map, as indicated by the absence of Mo, Ti, Al, and C. The age-hardened sample (Figure 34) shows concentrations of Cr, Mo, and Mn along the grain boundaries, suggesting the presence of (Cr, Mo, Mn)$_{23}C_6$ carbides.

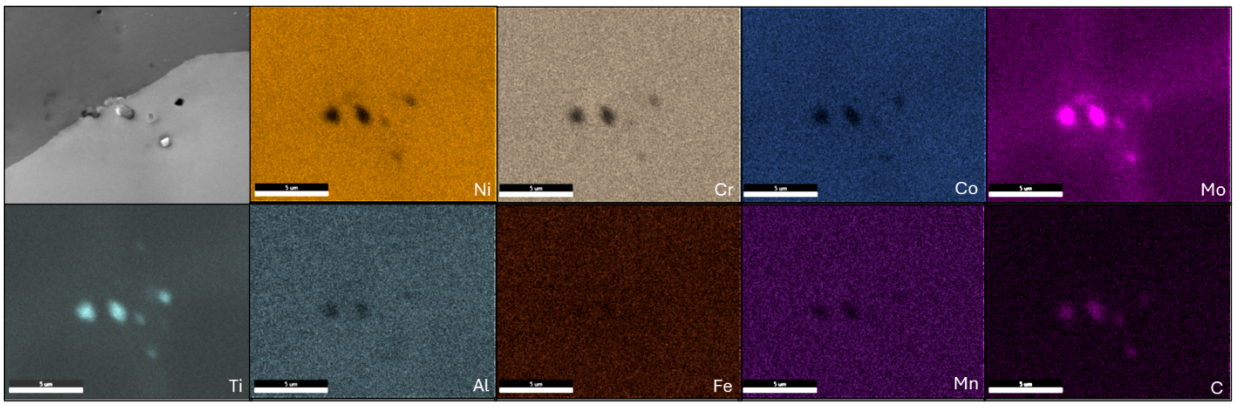

Figure 32. SEM EDS map at 20,000× magnification showing elemental distribution around grain boundary of as-deposited HY282 sample fabricated by GMA-DED.

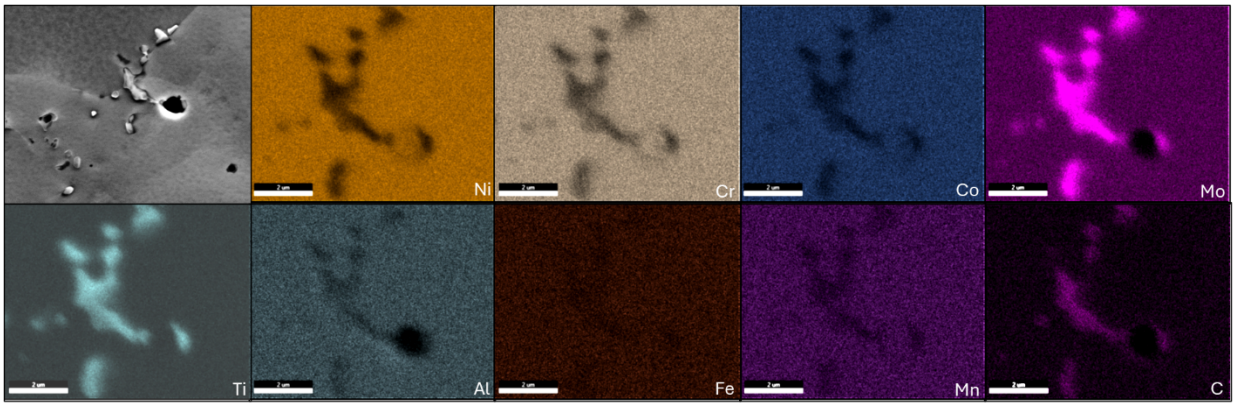

Figure 33. SEM EDS map at 20,000× magnification showing elemental distribution around grain boundary of solution-annealed HY282 sample fabricated by GMA-DED.

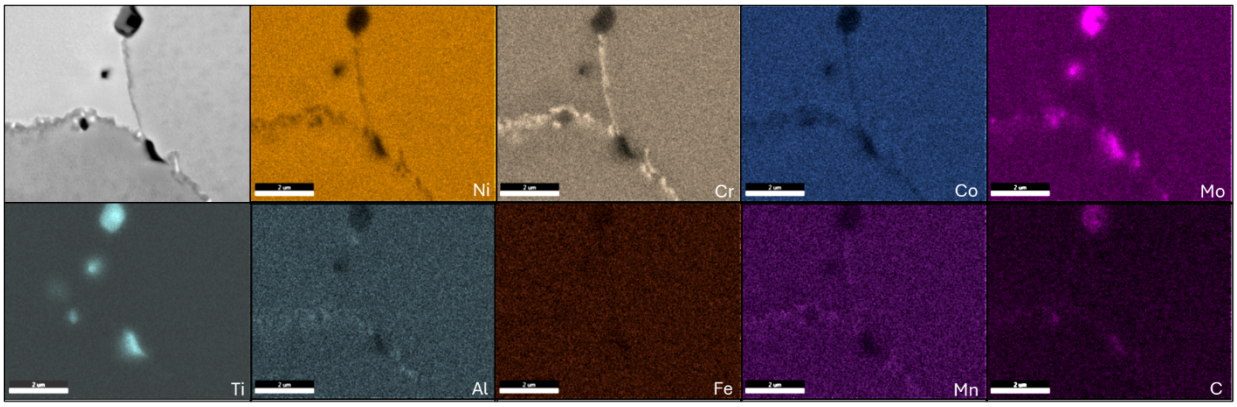

Figure 34. SEM EDS map at 20,000× magnification showing elemental distribution around grain boundary of age-hardened HY282 sample fabricated by GMA-DED.

Low-magnification SEM imaging, shown in Figure 35, of Haynes 282 fabricated by GMA-DED shows incomplete recrystallization during the heat treatment process. The heat treatment performed on samples fabricated by GMA-DED consisted of solution-annealing at 1,180°C for 1 h, followed by air-cooling and age-hardening at 800°C for 4 h, then air-cooling again. Nitrides, as shown in Figure 36, up to 10 µm in diameter were present in Haynes 282 fabricated by GMA-DED in all three states: as-deposited, solution-

annealed, and age-hardened. The Ti in the Haynes 282 reacts with nitrogen (N_2) at elevated temperatures when processed in a Ni-rich environment.

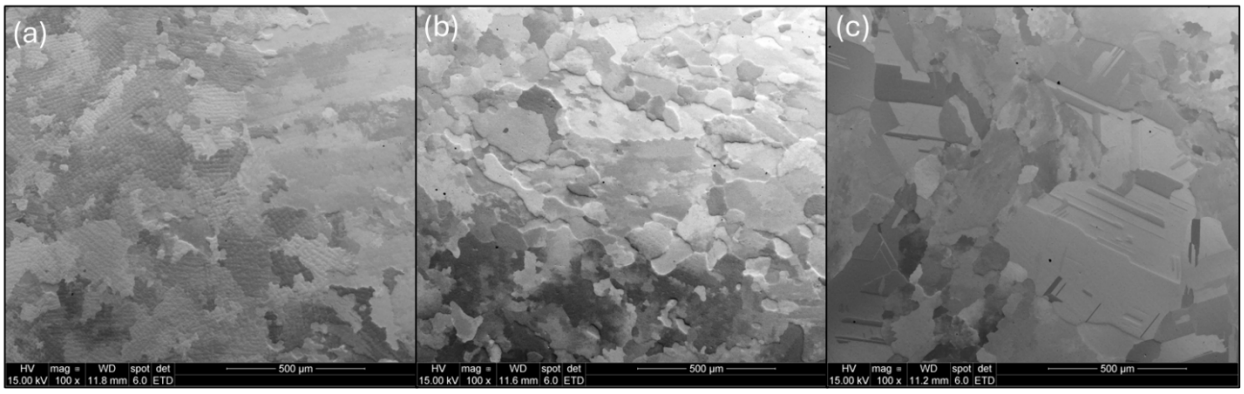

Figure 35. Low-magnification SEM imaging showing grain morphology of (a) as-deposited, (b) solution-annealed, and (c) age-hardened HY282 sample fabricated by GMA-DED.

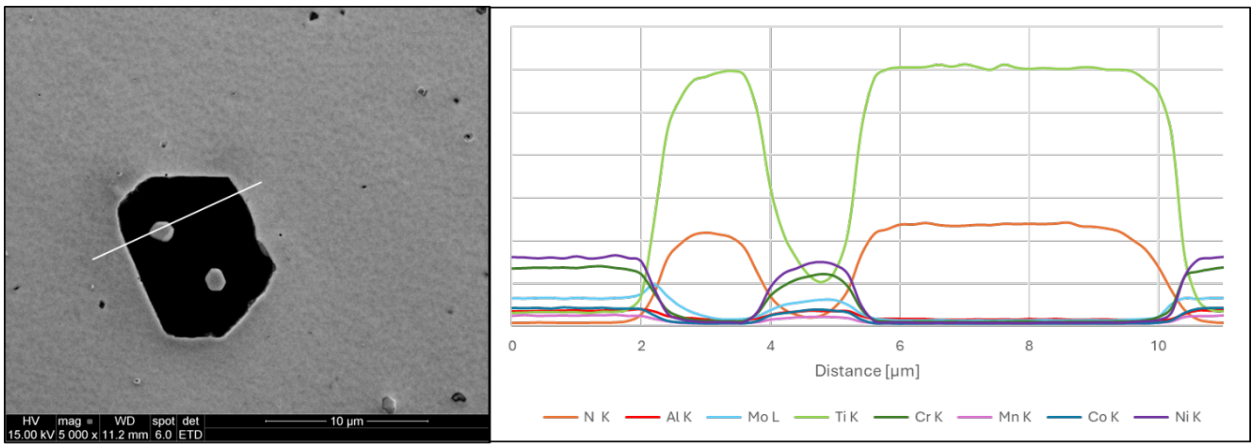

Figure 36. EDS line scan of TiN present in age-hardened HY282 fabricated by GMA-DED.

Figure 37 shows EDS line scans across several features present in the age-hardened sample. Line 1 across the Laves phase shows a significant increase in Mo and Ti with a corresponding decrease in Ni and Cr. The scan also shows a slight increase in N and C, suggesting the presence of carbides and nitrides. Line 2 across the grain boundary shows a decrease in Ni with an increase in Cr, Mo, and Mn, verifying the EDS map results in Figure 34. Line 3 across a secondary phase located at the grain boundary matches the composition change in line 1, suggesting the presence of carbides and nitrides along the grain boundary.

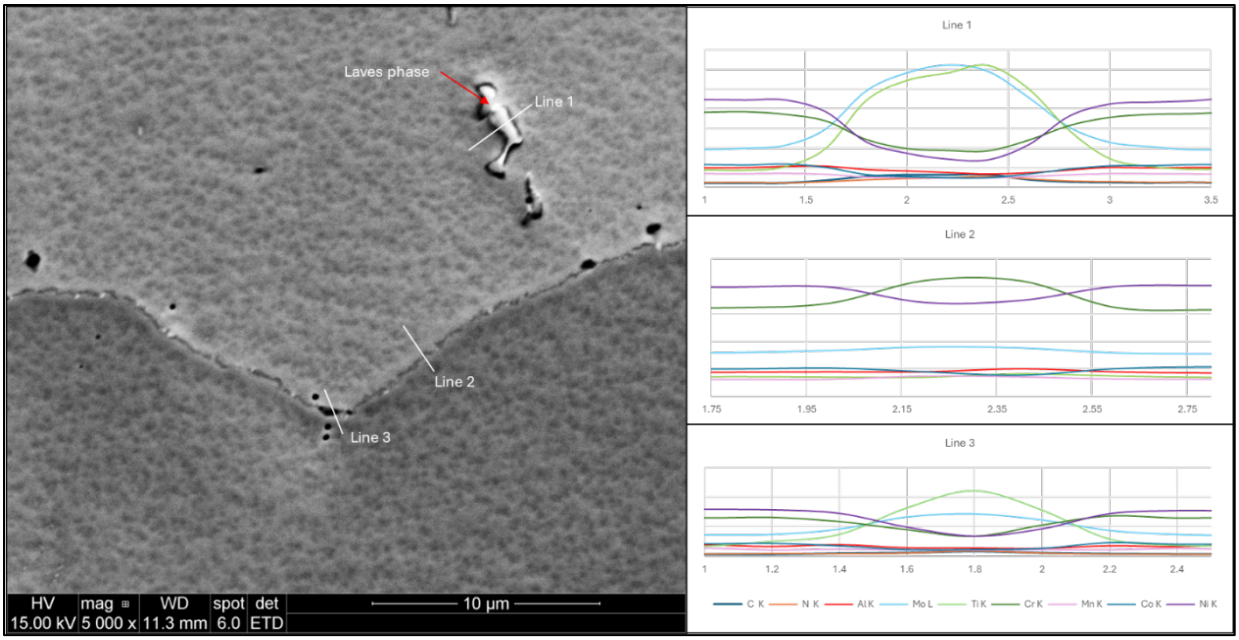

Figure 37. EDS line scans on grain boundary and Laves phase in age-hardened HY282 fabricated by GMA-DED.

3.4 CONCLUSION ON ADDITIVE MANUFACTURING 282

Alloy 282 is a compelling alloy because of its superior creep strength and powder availability. Although the alloy is known to be printable because of the relatively low Ti and Al content [37], the results of this work highlight the need for a careful printing strategy to avoid flaws in the final build that affect the alloy's mechanical properties. Although optimization of the LPBF 282 printing parameters resulted in a high-density alloy, a significant volume fraction of flaws was observed in the large LPBF 282 builds, especially for the build provided to INL, leading to low creep strength and ductility. Further optimization of the build strategy would be needed to reduce the flaw fraction and improve the creep properties. In addition to flaw control, controlling the microstructure through optimization of the heat treatment is challenging. The 1 h, 1180°C heat treatment that led to full recrystallization for the LPBF 282 specimen resulted in partial recrystallization of the LPBF ORNL material, with significant variation from one specimen to another. Ongoing work aims at the characterization of the alloy γ′ precipitates in the bulk and carbides at grain boundaries to better understand the lower performance of the LPBF 282 alloy.

This work has also demonstrated that the use of in situ data and XCT scans can provide crucial information to establish a correlation between the printed microstructure and the LPBF 282 creep properties. Such an approach is at the center of the AMMT program and will be further integrated into the LPBF 625 fabrication and qualification. The different degrees of flaw densities were shown to have a significant effect on creep properties, with caused the LPBF 282 alloy to exhibit low creep strength and ductility compared with wrought 282.

LP-DED samples were fabricated with minimal volumetric defects and no significant compositional change, as described in Table 4. XRD analysis showed the presence of γ, γ′, and η phases as well as MC and $M_{23}C_6$ carbides. EDS analysis along grain boundaries in the as-deposited, solution-annealed, and age-hardened samples confirmed the presence of these carbides. Because of their small size, MC carbides are not typically detectable in XRD analysis, suggesting that the volume fraction present may be higher in the LP-DED samples than in material fabricated by other methods. This higher volume fraction could be the cause of the notably higher hardness values for the LP-DED samples at 361 HV compared with 263 HV

for cast HY282. EBSD analysis shows incomplete recrystallization during the heat treatment process, suggesting that alternative processes should be explored for HY282 fabricated by LP-DED. The GMA-DED samples also showed incomplete recrystallization during the heat treatment process. A high volume of secondary carbide and nitride phases were indicated in SEM and EDS analysis. SEM images of heat-treated sample showed γ′ precipitates and the presence of Laves phases and spherical porosity from gas entrapment. Additional characterization work is still being conducted on samples fabricated by GMA-DED. Cyclic and creep testing are planned for material from both DED processes. Cyclic and creep testing are planned for material from both DED processes. All these results indicate that the three AM techniques investigated in this report can result in high-density Ni-based alloys with potential use in nuclear reactors at $T > 700°C$. Further optimization of the printing strategies and heat treatment is necessary to achieve properties approaching the properties of conventional alloys.

4. LOW-CHROMIUM MOLTEN SALT–COMPATIBLE ALLOYS

The previous report highlighted low-Cr Hastelloy N and Haynes 244 as the two key Ni-based alloy candidates for components requiring compatibility with molten salt at $T > 700°C$ [8]. Although wrought Hastelloy N is a well-known alloy designed for molten salt applications [21] and has a large, relevant database already generated, and alloy 244 is a more recent alloy with limited available data, but as shown in Figure 1, the creep properties of the alloy are drastically superior to the creep properties of Hastelloy N. To help with alloy selection, INL initiated the compatibility evaluation of alloy 244 in molten salts, and ORNL focused on the alloy printability using single-track experiments on wrought Hastelloy N and 244.

4.1 SINGLE-TRACK EXPERIMENT AND PRINTABILITY ASSESSMENT

In total, 17 individual scans were carried out on alloy Hastelloy N, and 14 were performed on alloy 244; a summary of the printing parameters is given in Table 10. Three key parameters were evaluated: laser power, point distance, and dwell time resulting in linear density and resulting in a linear energy density varying from 0.45 to 1.19 J/mm. Additionally, one set of three overlapping scans was produced with a laser power of 350 W, a point distance of 70 µm, a dwell time of 70 ms, and a hatch distance of 100 µm. An optical top view of the Hastelloy N and 244 specimens after the single-track experiments is shown in Figure 38.

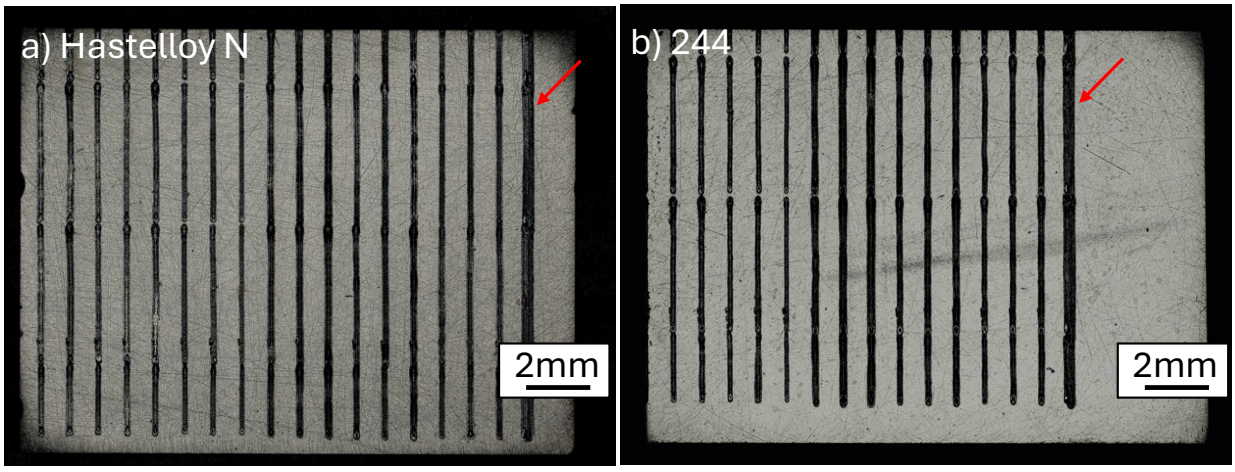

Figure 38. Top view optical images of the single-track coupons: (a) Hastelloy N and (b) alloy 244. Red arrows highlight two sets of three overlapping scans.

Representative cross-sectional optical micrographs of the melted areas are displayed in Figure 39 for the Hastelloy N and 244 alloys. None of the laser printing conditions led to the formation of cracks in the melted area. The Hastelloy N mount was then etched to reveal microstructure features in the melted areas. As shown in Figure 40, a typical LPBF cellular structure was observed with the shape and depth of penetration of the melted areas directly related to the linear energy density.

Table 10. Parameters for the single-track experiments on Hastelloy N and 244 alloys

Number	Laser power (W)	Point distance (µm)	Dwell time (µs)	Scan speed (mm/s)	Energy density (J/mm)
1, HN	350	50	90	500.0	0.7
2, HN	350	50	100	454.5	0.77
3, HN	350	60	80	666.7	0.525
4, HN & 244	350	60	90	600.0	0.583333333
5, HN & 244	350	60	100	545.5	0.641666667
6, HN & 244	350	70	80	777.8	0.45
7, HN & 244	350	70	90	700.0	0.5
8, HN & 244	250	70	100	636.4	0.392857143
9, HN & 244	250	40	140	266.7	0.9375
10, HN & 244	250	40	160	235.3	1.0625
11, HN & 244	250	40	180	210.5	1.1875
12, HN & 244	250	50	140	333.3	0.75
13, HN & 244	250	50	160	294.1	0.85
14, HN & 244	250	50	180	263.2	0.95
15, HN & 244	250	60	140	400.0	0.625
16, HN & 244	250	60	160	352.9	0.708333333
17, HN & 244	250	60	180	315.8	0.791666667
18, HN & 244	350	70	100	636.4	0.55

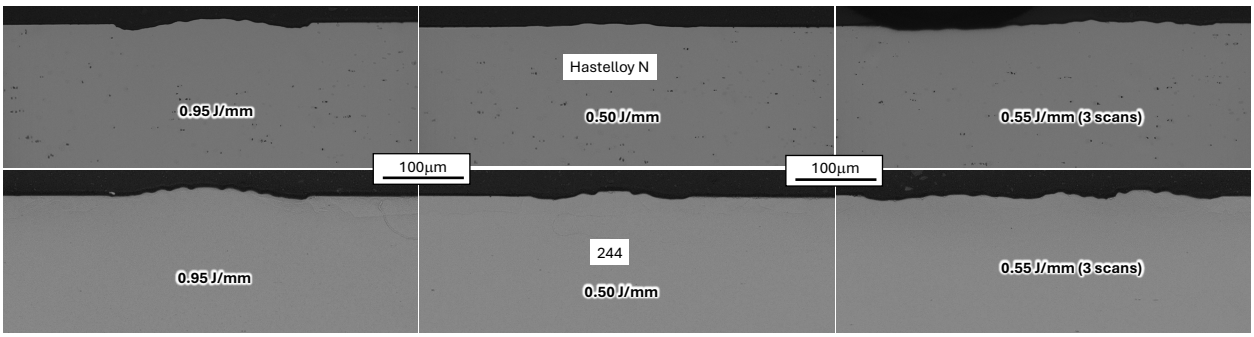

Figure 39. Micrographs highlighting the absence of cracks in the melted areas of the single-track experiments for alloy Hastelloy N and 244.

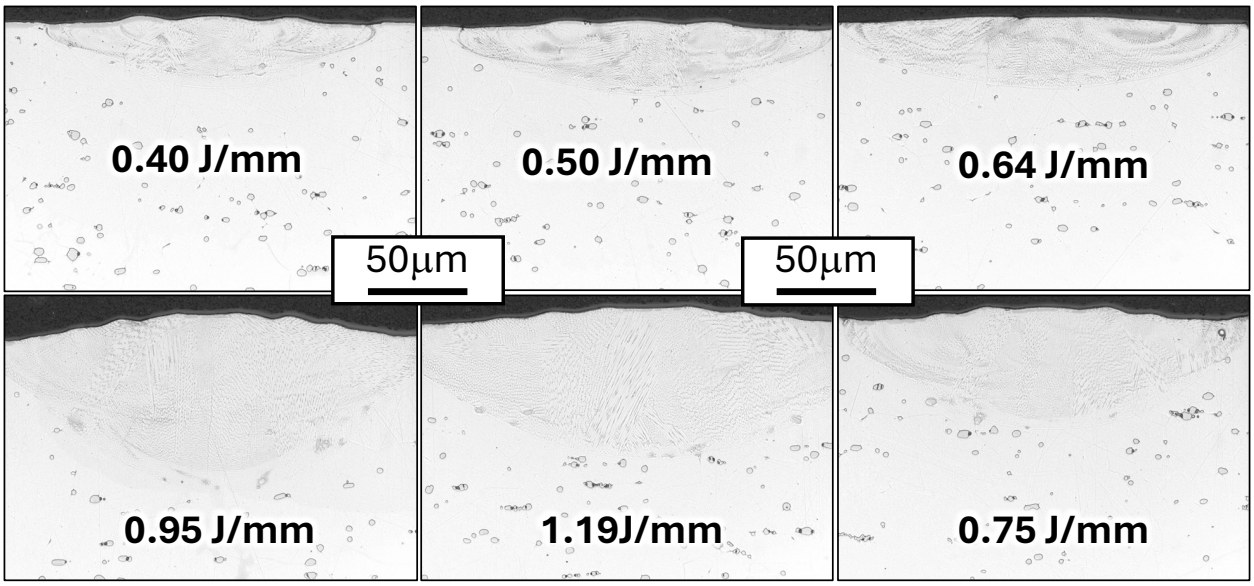

Figure 40. Micrographs highlighting the presence of a cellular structure in the melted areas of the Hastelloy N single-track experiments.

4.2 MOLTEN SALT COMPATIBILITY EVALUTION

Static molten salt testing was performed on both alloys, as well as Alloy 625 and Haynes 282. All four material coupons were made from wrought material. A Ni wire was used to hang the coupons in glassy C crucibles, shown in Figure 41. Two separate tests were performed at 750°C for 1,000 h: one in NaCl–$MgCl_2$ salt and one in LiF–NaF–KF (FLiNaK) salt. Some vaporization was noted in the NaCl–$MgCl_2$ test, so a second test was performed at 700 °C for 1,000 h. Weight loss, summarized in Table 11, was in the following order of more to less severe susceptibility to corrosion: Alloy 625 > Haynes 282 > Haynes 244 ≈ Hastelloy N. It should be noted that not all coupons were the same size, so weight loss is not a perfect metric for comparison. After the corrosion tests, the coupons from the second NaCl–$MgCl_2$ and the FLiNaK tests were cross sectioned. The average corrosion depth is noted in Table 11. Differences between Hastelloy N and Haynes 244 were observed that are not readily apparent from the summary provided in Table 11. Figure 42 through Figure 45 show cross sections and EDS maps of chromium depletion. While it is true there is visible, fairly uniform corrosion at the surface of Haynes 244, the EDS maps show irregular depletion in the Hastelloy N, with occasional deep depletion of chromium in both NaCl–$MgCl_2$ and the FLiNaK. So while Hastelloy N does appear to be more resistant to molten salt corrosion, Haynes 244 is also a very good choice for a molten salt alloy.

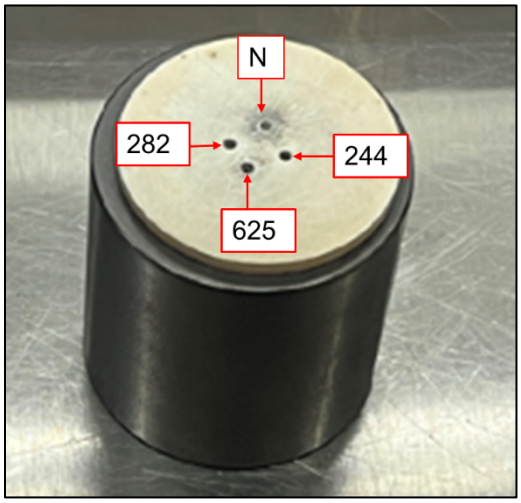

Figure 41. Static molten salt corrosion capsule.

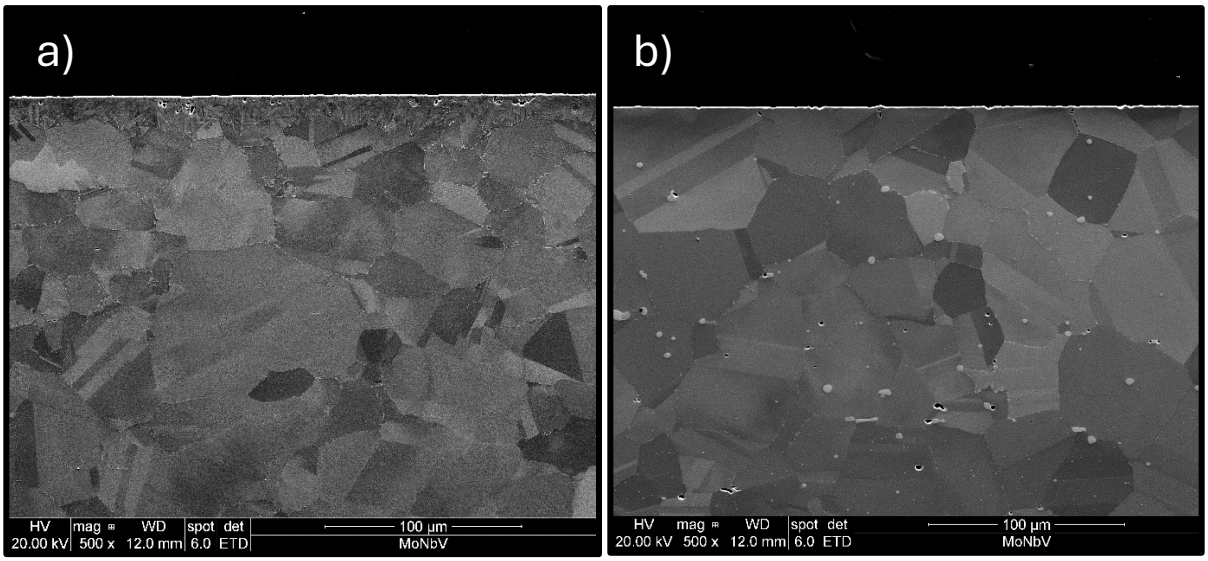

Figure 42. Cross sections of (a) Haynes 244 and (b) Hastelloy N after 1,000 NaCl–$MgCl_2$ test showing Cr depletion.

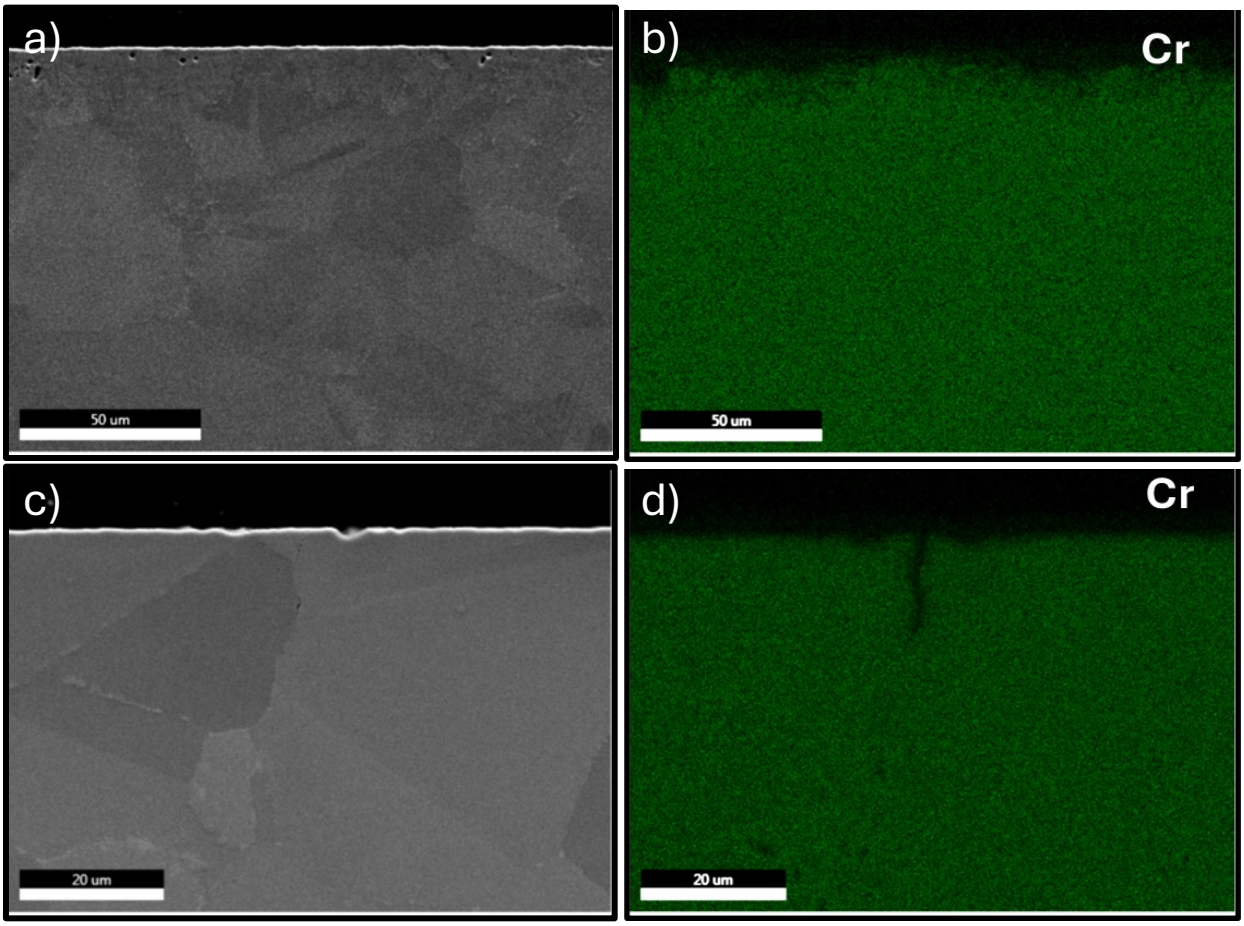

Figure 43. SEM and corresponding EDS Cr maps after a 1,000 h exposure in NaCl–$MgCl_2$: (a) and (b) Haynes 244 and (c) and (d) Hastelloy N.

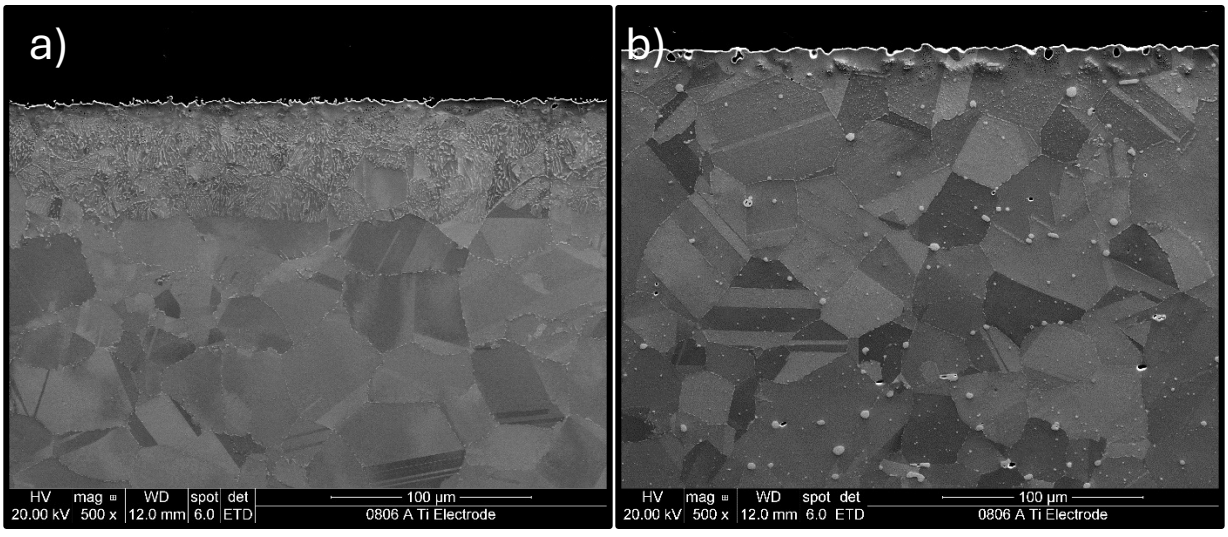

Figure 44. Micrographs after exposure for 1,000 h in FLiNaK: (a) Haynes 244 and (b) Hastelloy N.

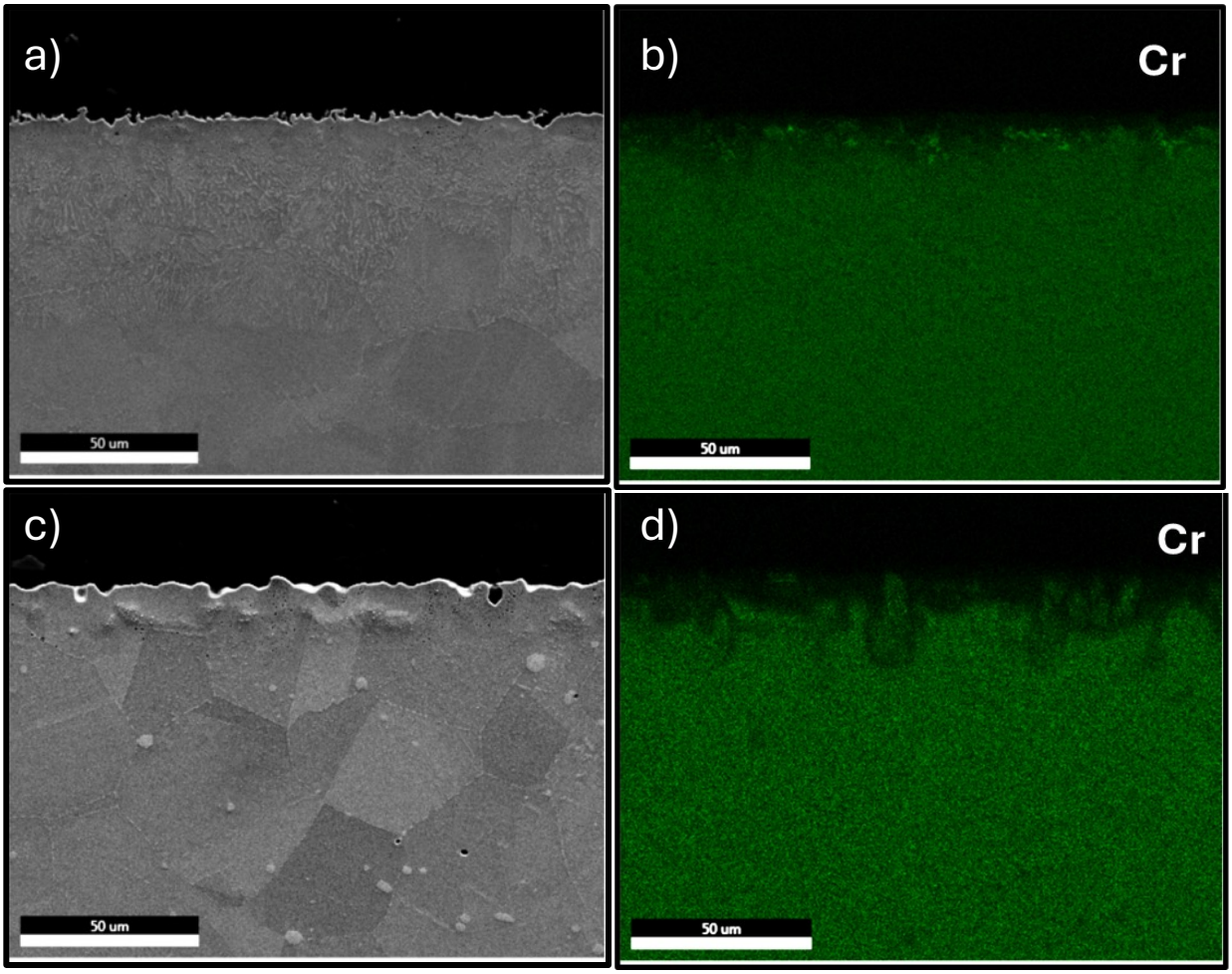

Figure 45. SEM and corresponding EDS maps after exposure for 1,000 h in FLiNaK: (a) and (b) Haynes 244 and (c) and (d) Hastelloy N.

Table 11. Summary of corrosion results from static molten salt experiments

Test parameters	Specimen ID	Pretest		Post-test		Weight change ratio (%)	Average corrosion depth (μm)
		Mass (g)	Avg Mass (g)	Mass (g)	Avg Mass (g)		
$NaCl–MgCl_2$, 750°C, 1,000 h	625-A	0.4570	0.4571	0.4392	0.4392	−3.90	—
		0.4570		0.4392			
		0.4572		0.4393			
	282-A	0.4929	0.4929	0.4870	0.4870	−1.19	—
		0.4929		0.4870			
		0.4928		0.4870			
	244-A	0.9197	0.9196	0.9185	0.9185	−0.13	—
		0.9197		0.9185			
		0.9195		0.9184			
	N-A	0.4909	0.4908	0.4903	0.4903	−0.10	—
		0.4908		0.4903			
		0.4908		0.4903			
$NaCl–MgCl_2$, 700°C, 1,000 h	625-C	0.5171	0.517	0.4996	0.4995	-3.38	110
		0.517		0.4995			
		0.517		0.4995			
	282-C	0.5695	0.5695	0.567	0.5671	-0.42	49
		0.5695		0.567			
		0.5694		0.5672			
	244-C	1.0797	1.0798	1.0815	1.0814	0.15	20
		1.0798		1.0814			
		1.0798		1.0814			
	N-C	0.5925	0.5925	0.5929	0.5930	0.08	~0
		0.5925		0.5930			
		0.5925		0.5930			
FLiNaK, 750°C, 1,000 h	625-B	0.4879	0.4878	0.4283	0.4283	−12.21	375
		0.4879		0.4283			
		0.4877		0.4282			
	282-B	0.4934	0.4935	0.4782	0.4782	−3.09	280
		0.4935		0.4782			
		0.4935		0.4783			
	244-B	0.9151	0.9152	0.9131	0.9131	−0.23	60
		0.9153		0.9131			
		0.9153		0.9131			
	N-B	0.4839	0.4838	0.4825	0.4825	−0.27	15
		0.4839		0.4825			
		0.4836		0.4825			

5. CONCLUSION

To select Ni-based alloys relevant to the AMMT program and the NE industry, work was performed on low-Co 625 alloy; high-temperature, high-strength 617, 230, and 282 alloys; and low-Cr molten salt–compatible Hastelloy N and 244 alloys. Printing of crack-free 617 and 230 by LPBF could not be achieved because of hot tearing, and composition changes would likely be needed. Although alloy 230 exhibited great room-temperature tensile properties along the BD with very high yield strength, ductility was significantly reduced perpendicular to the BD because of the presence of cracks. As expected, the fabrication of crack-free LPBF 625 using similar printing parameters was achieved, highlighting the excellent printability of the alloy. The growing interest in alloy 625 from the NE community, its satisfactory high-temperature strength and corrosion resistance, and the excellent alloy printability make LPBF 625 a promising alloy for the AMMT program, and extensive characterization of 625 produced by AM will be the focused in FY 2025. The γ′-strengthened alloy 282 was produced by LPBF at ORNL and by LP-DED and GMA-DED at INL. In all cases, materials with a low density of flaws could be produced, but heat treatments need to be optimized to obtain full recrystallization of the alloys. The production at ORNL of larger LPBF builds for mechanical testing resulted in drastic variation in flaw density from one rod to another, highlighting the importance of printing strategies even if optimized parameters have been identified. XCT scans were used to establish a correlation between LPBF specimen flaws and creep properties, but the low creep strength and ductility of the LPBF 282 alloy compared with wrought 282 are also related to differences in grain structure and phases present in the alloy. The γ' precipitates in the bulk and carbides at grain boundaries were identified at INL in the LP-DED 282 alloy, and extensive characterization will be performed to compare the microstructure of the AM 282 alloys with the microstructure of wrought 282. Based on the work conducted on AM 282, a strategy to accelerate the fabrication and qualification of AM 625 will be proposed in FY 2025. Finally, single-track experiments conducted on wrought Hastelloy N and alloy 244 at ORNL did not reveal any cracking susceptibility for either of the two alloys, and preliminary corrosion results showed similar molten salt resistance for alloy 244 and Hastelloy N. The very high strength of alloy 244 at a high temperature might open new opportunities for the fabrication of molten salt reactor components, and the printability of the alloy will be further explored.

6. REFERENCES

1. I. Gibson, D. Rosen, B. Stucker, M. Khorasani, *Additive Manufacturing Technologies*, Vol. 17 (Springer, 2021).
2. B. R. Betzler, B. J. Ade, P. K. Jain, A. J. Wysocki, P. C. Chesser, W. M. Kirkland, M. S. Cetiner, A. Bergeron, F. Heidet, and K. A. Terrani, "Conceptual Design of the Transformational Challenge Reactor," *Nuclear Science and Engineering* 196 (2022): 1399–1424.
3. J. Haley, C. Leach, B. Jordan, R. Dehoff, and V. Pacquit, "In-Situ Digital Image Correlation and Thermal Monitoring in Directed Energy Deposition Additive Manufacturing," *Optics Express* 29, no. 7 (2021): 9927–9941.
4. A. Huning. A. Smith, L. Scime, M. Russell, A. Coates, V. Paquit, and R. Dehoff, *Advancement of Certification Methods and Applications for Industrial Deployments of Components Derived from Advanced Manufacturing Technologies*, ORNL/TM-2022/2654 (Oak Ridge, Tennessee: Oak Ridge National Laboratory, 2022).
5. M. Li, D. Andersson, R. Dehoff, A. Jokisaari, I. Van Rooyen, and D. Cairns-Gallimore, *Advanced Materials and Manufacturing Technologies (AMMT), 2022 Roadmap*, ANL-23/12 (Lemont, Illinois: Argonne National Laboratory, 2022).

6. A. Ziabari, et al., *Report Outlining Computed Tomography Strategy and Microscopy Approach to Qualifying AM 316 Materials*, ORNL/TM-2023/3016 (Oak Ridge, Tennessee: Oak Ridge National Laboratory, 2023).

7. X. Zhang, S. A. Mantri, G. I. Vukovic, J. Listwan, D. Rink, and E. Listwan, *Development of Process Parameters and Post-Build Conditions for Qualification of LPBF 316 SS*, ANL-AMMT-004 (Lemont, Illinois: Argonne National Laboratory, 2023).

8. S. Dryepondt et al., *Prioritization of Existing Reactor Materials, 2023*, ORNL/TM-2023/3108 (Oak Ridge, Tennessee: Oak Ridge National Laboratory, 2023).

9. M. Griffiths, "Chapter 9: Ni-Based Alloys for Reactor Internals and Steam Generator Applications," in *Structural Alloys for Nuclear Energy Applications*, ed. G. R. Odette and S. J. Zinkle (Boston, Massachusetts: Elsevier, 2019).

10. GE Reports, "TURN UP: Larger, Lighter Additive Parts," GE Aerospace, Published December 13, 2022, https://www.geaerospace.com/news/articles/manufacturing-product/turn-larger-lighter-additive-parts.

11. S. Dryepondt, S. Taller, Z. Snow, H. Hyer, A. Ziabari, and Y-F. Su, *Complete Optimization of LPBF Ni-Based Alloys Down-Selected from FY23 Candidate Materials Including Thermodynamic Modeling, Sample Fabrication and Microstructure Characterization*, ORNL/TM-2024/3464 (Oak Ridge, Tennessee: Oak Ridge National Laboratory, 2024).

12. R. Wright, *Draft ASME Boiler and Pressure Vessel Code Cases and Technical Bases for Use of Alloy 617 for Constructions of Nuclear Component Under Section III, Division 5*, INL/EXT-15-36305 Revision 2 (Idaho Falls, Idaho: Idaho National Laboratory, 2021).

13. T. Hassel1 and T. Carstensen, "Properties and Anisotropy Behaviour of a Nickel Base Alloy Material Produced by Robot-Based Wire and Arc Additive Manufacturing," *Welding in the World* 64 (2020): 1921–1931.

14. B. Avinash , K. Manikanda Subramanian, and V. Rajkumar, "Microstructure, Mechanical Properties and Corrosion Behavior of Inconel 617 Superalloy Fabricated by Wire Arc Additive Manufacturing," *Journal of Materials Engineering and Performance* 32 (2023): 6270–6280.

15. "HAYNES 230 Alloy: Principal Features," Haynes International, https://haynesintl.com/en/datasheet/haynes-230-alloy/.

16. Y. Zhao, Z. Ma, L. Yu, and Y. Liu, "New Alloy Design Approach to Inhibiting Hot Cracking in Laser Additive Manufactured Nickel-Based Superalloys," *Acta Materialia* 247 (2023): 118736.

17. X. Liu, R. Hu, X. Luo, C. Yang, and X. Gao, "A High-Strength Ni–Cr–W Based Superalloy Prepared by Laser Powder Bed Fusion: Printability, Microstructure and Tensile Properties," *Materials Science and Engineering A* 853 (2022): 143744.

18. K. Momeni, "Sensitivity of Laser Powder Bed Fusion Additive Manufactured HAYNES230 to Composition and Print Parameters," *Journal of Materials Research and Technology* 15 (2021): 6453–6463.

19. B. A. Pint, H. Wang, C. S. Hawkins, and K. A. Unocic, *Technical Qualification of New Materials for High Efficiency Coal-Fired Boilers and Other Advanced FE Concepts: Haynes 282 ASME Boiler and Pressure Vessel Code Case*, ORNL/TM-2020/1548 (Oak Ridge, Tennessee: Oak Ridge National Laboratory, 2020).

20. C. Magnin, Z. Islam, M. Elbakhshwan, A. Brittan, D. J. Thoma, and M. H.Anderson, "The Performance of Additively Manufactured Haynes 282 in Supercritical CO_2," *Materials Science and Engineering A* 841 (2022): 143007.

21. R. W. Swindeman, *The Mechanical Properties of INOR-8*, ORNL-2780 (Oak Ridge, Tennessee: Oak Ridge National Laboratory, 1961).

22. "Haynes 244 Alloy," Haynes International Corporation, https://haynesintl.com/en/datasheet/haynes-244-alloy/.

23. "Haynes 625 Alloy," Haynes International Corporation, https://haynesintl.com/en/datasheet/haynes-625-alloy/.

24. N. J. Harrison, I. Todd, and K. Mumtaz, "Reduction of Micro-Cracking in Nickel Superalloys Processed by Selective Laser Melting: A Fundamental Alloy Design Approach," *Acta Materialia* 94 (2015): 59–68.

25. G. Marchese, G. Basile, E. Bassini, A. Aversa, M. Lombardi, D. Ugues, P. Fino, and S. Biamino, "Study of the Microstructure and Cracking Mechanisms of Hastelloy X Produced by Laser Powder Bed Fusion," *Materials* 11, no. 106 (2018).

26. D. Tomus, et al., "Controlling the Microstructure of Hastelloy-X Components Manufactured by Selective Laser Melting," *Physics Procedia* 41 (2013): 816–820.

27. A. Monson, M. Mulholland, T. Patterson, and M. McMurtrey, *Nuclear Structural Component Relevant Properties of Nickel-Based Alloys Produced via Additive Manufacturing*, INL/RPT-24-80220 (Idaho Falls, Idaho: Idaho National Laboratory, 2024).

28. A. Ziabari et al. "Enabling Rapid X-Ray CT Characterization for Additive Manufacturing Using CAD Models and Deep Learning-Based Reconstruction," *npj Computational Materials* 9, no. 91 (2023).

29. ASTM International, *Standard Test Methods for Conducting Creep, Creep-Rupture, and Stress-Rupture Tests of Metallic Materials*, ASTM E139-11 (2018).

30. M. C. Messner, B. Barua, and M. D. McMurtrey, srlife: A Fast Tool for High Temperature Receiver Design and Analysis, ANL-22/29 (Argonne, Illinois, Argonne National Laboratory, 2022).

31. N. Dudova, A. Belyakov, T. Sakai, and R. Kaibyshev, "Dynamic Recrystallization Mechanisms Operating in a Ni-20% Cr Alloy under Hot-to-Warm Working," *Acta Materialia* 58, no. 10 (2010): 3624–3632.

32. Y. Yang, R. C. Thomson, R. M. Leese, and S. Roberts, "Microstructural Evolution in Case Haynes 282 for Application in Advanced Power Plants," *Advances in Materials* 84666 (2013): 143–154.

33. A. Polkowska, W. Polkowski, M. Warmuzek, N. Cieśla, G. Włoch, D. Zasada, and R. M. Purgert, "Microstructure and Hardness Evolution in Haynes 282 Nickel-based Superalloy during Multi-Variant Aging Heat Treatment," *Journal of Materials Engineering and Performance* 28 (2019): 3844–3851.

34. S. Haas, J. Andersson, M. Fisk, J.-S. Park, and U. Lienert, "Correlation of Precipitate Evolution with Vickers Hardness in Haynes 282 Superalloy: In-situ High-energy SAXS/WAXS Investigation," *Materials Science and Engineering A* 711 (2018): 250–258.

35. A. Ramakrishnan and G. P. Dinda, "Microstructure and Mechanical Properties of Direct Laser Metal Deposited Haynes 282 Superalloy," *Materials Science and Engineering A* 748 (2019): 347–356.

36. K. Hou, M. Ou, W. Xing, G. Ma, X. Hao, M. Wang, and Y. Ma, "The Formation of η-Ni3Ti Phase Microstructure in a Cast Nickel-based Superalloy with High Ti/Al Ratio," *Journal of Materials Research and Technology* 29 (2024): 764–778.

37. L. M. Pike, “Development of a Fabricable Gamma-Prime (γ′) Strengthened Superalloy,” in *Superalloys*, ed. R. C. Reed, K. A. Green, P. Caron, T. P. Gabb, M. G. Fahrmann, E. S. Huron, and S. A. Woodard, 191–200 (TMS [The Minerals, Metals and Materials Society], 2008.